International Journal of Heat and Mass Transfer 216 (2023) 124604

Contents lists available at ScienceDirect

International Journal of Heat and Mass Transfer

journal homepage: www.elsevier.com/locate/ijhmt

Investigating the performance of conventional and hydrophobic surface heat sink in managing thermal challenges of high heat generating components

Hamza Babar [a,*], Hongwei Wu [a], Wenbin Zhang [b]

[a] School of Physics, Engineering and Computer Science, University of Hertfordshire, Hatfield AL10 9AB, United Kingdom
[b] School of Science and Technology, Nottingham Trent University, Clifton Lane, Nottingham NG11 8NS, United Kingdom

ARTICLE INFO

Keywords:
Heat sink
Liquid-cooling
Hydrophobic surface
Electronics
Thermal management

ABSTRACT

In the pursuit of optimizing heat dissipation and improving performance in electronic devices, liquid-cooled heat sinks have garnered significant interest due to their potential to improve heat transfer efficiency. Presented study set out to assess the effectiveness of straight channel heat sinks as a thermal solution for high heat generating electronics components, while also investigating the impact of applying a hydrophobic coating on their performance. A series of tests were conducted at different heating powers (50W-250 W) and flow rates (200–950 ml/min), while also considering different orientations and directions of flow. The investigation focused on analysing critical aspects such as heat transfer performance, wall temperature variations, thermal resistance, and pressure drop characteristics of straight channel heat sinks with conventional and hydrophobic-coated surfaces. The results showed that the Nusselt number increased with higher Reynolds numbers and heating powers, indicating improved heat transfer efficiency. However, the hydrophobic coating on the heat sink surface led to a reduction in the Nusselt number due to the formation and retention of bubbles, hindering heat transfer. The maximum average reduction of 20.85% in Nusselt number was noticed at 100 W for the vertically positioned hydrophobic-coated heat sink with downward flow compared to conventional surface (CS) heat sink. Additionally, the findings revealed that pressure drop is influenced by Reynolds number and the presence of bubbles, with gravity playing a role in reducing pressure drop in certain orientations. A hydrophobic coating shows a small decrease in pressure drop, but bubble formation limits its effectiveness to some extent. Comparisons also indicated that the highest average decrease in pressure drop about 11.92% was observed for the same configuration, vertically positioned hydrophobic heat sink with downward flow, at 50 W. Moreover, the study's findings have broader implications beyond electronics. Heat sinks are widely employed in various industries, including automotive, aerospace, renewable energy systems, and industrial processes.

1. Introduction

Maintaining optimal operating temperatures is critical in numerous fields and applications. In electronics, such as computer processors, graphics cards, and power electronics, excessive heat can cause performance degradation and even lead to component failure. As we venture into the future, the advancement of artificial intelligence (AI) continues to drive an increased demand for more efficient and sophisticated cooling systems in data centres and AI hardware infrastructure. amongst various liquid cooling methods, the implementation of liquid-cooled heat sinks has gained significant attention. Liquid cooling emerges as a highly auspicious technique for effectively dissipating heat generated by electronic devices, owing to its commendable attributes such as a significantly elevated thermal conductivity and unparalleled prowess in facilitating heat transfer. In this context, water has emerged as an effective working fluid owing to its excellent heat transfer properties, low cost, and environmental friendliness. Straight-channel heat sinks are favoured in numerous cooling applications, such as electronic devices and thermal management systems, due to their ease of manufacturing, cost-effectiveness, and efficient resource utilization. Moreover, their design allows for easy extension by adding more channels to enhance cooling capabilities further. Improving heat transfer efficiency is crucial to enhance the performance of these heat sinks. Indeed, heat sinks have been combined with various cooling systems like phase change materials, thermoelectric coolers, heat pipes, etc., to

* Corresponding author.
E-mail addresses: h.babar@herts.ac.uk (H. Babar), h.wu6@herts.ac.uk (H. Wu), wenbin.zhang@ntu.ac.uk (W. Zhang).

https://doi.org/10.1016/j.ijheatmasstransfer.2023.124604
Received 25 July 2023; Received in revised form 10 August 2023; Accepted 11 August 2023
Available online 18 August 2023

Nomenclature

AI	*Artificial intelligence*
CS	*Conventional surface*
CNC	*Computer Numerical Control*
CPU	*Central processing unit*
Cu	*Copper*
DW	*Deionized water*
HS	*Hydrophobic surface*
HTC	*Heat transfer coefficient*
LMTD	*Logarithmic mean temperature difference*
MAE	*Mean absolute error*
MCHS	*Mini channel heat sink*
MgO	*Magnesium oxide*
TiO_2	Titanium *dioxide, Titania*

Symbols

A	*Cross sectional area* $[m^2]$
AR	*Aspect ratio*
C_p	*Heat capacity* $[J/kg\ ^\circ C]$
D	*Diameter* $[m]$
d_h	*Hydraulic diameter* $[m]$
h	*Channel height* $[m]$
h_{conv}	*Heat transfer coefficient* $[W/m^2\ ^\circ C]$
k	*Thermal conductivity* $[W/m\ ^\circ C]$
L_s	*Channel length* $[m]$
m	*Mass flow rate* $[kg/s]$
P	*Wetted parameter*
ΔP	*Pressure drop* $[Pa]$
Pr	*Prandtl number*
Q	*Heat transfer rate* $[W]$
R_{th}	*Thermal Resistance* $[m^2\ ^\circ C/W]$
Re	*Reynolds number*
T	*Temperature* $[^\circ C]$
t	*Number of channels*
$x_{exp.}$	*Experimental quantity*
$x_{pred.}$	*Predicted quantity*
V	*Volumetric flow rate* $[m^3/s]$
v	*Fluid velocity* $[m/s]$
W	*Channel width* $[m]$
W_s	*Width of finned part* $[m]$

Greek Letter

ρ	*Density* $[kg/m^3]$
μ	*Viscosity* $[kg/m.s]$

Subscript

b	*Base*
eff	*Effective*
f	*Fin*
w	*Wall*

enhance heat dissipation and improve overall thermal management in electronic devices and other applications [1–3]. Jang et al. [4] investigated the thermal performance of heat pipe integrated heat sink for battery thermal management systems. The results showed that the hybrid system outperformed simple liquid cooling, particularly at higher discharge rates and flow rates.

The study conducted by Wu et al. [5] demonstrated the potential of using 3D-printed tree-shaped mini-channels for high performance chip cooling. The sink was constructed using aluminium alloy, considering the principles of constructal theory to enhance fluid flow and heat transfer through its four levels of branching mini-channels. A number of tests were run to investigate the impact of coolant flow rate and heat flux on the performance of heat sink, revealing its effectiveness in cooling chips with average surface temperature ranging from 23.8 °C to 66.6 °C at heat flux of 5–8 W/cm^2. Interestingly, it was observed that the surface temperatures increased at very high flow rates above 0.073 m^3/h. The investigators hypothesize this is due to flow disturbance at the mini-channel bifurcations. Gorzin et al. [6] investigated a novel serpentine mini-channel heat sink (MCHS) for CPU liquid cooling. The heat sink, made of aluminium, square cross-section channels with a depth and width of 2 mm, and utilized pure water as the coolant fluid. The study examined the impact of varying mass flow rates and inlet temperatures on the heat sink's efficiency. The results of the experiments revealed that the proposed serpentine "maze" design outperformed a conventional straight channel design. It demonstrated up to an 11.2% reduction in baseplate temperature and an impressive up to 4.2 times increase in the Nusselt number, especially at the highest tested mass flow rate. The study also found that increasing the mass flow rate and reducing the inlet temperature positively influenced the heat sink's performance. Wang et al. [7] numerically investigated the influence of microchannel geometry on heat transfer and fluid flow, considering three cross-sectional shapes: rectangular, triangular, and trapezoidal. The findings revealed that in rectangular microchannels, increasing the aspect ratio (height to width ratio) leads to decreased thermal resistance but increased pressure drop. A comparison of the three shapes with the same hydraulic diameter showed that rectangular microchannels have the lowest thermal resistance, followed by trapezoidal and triangular channels. Additionally, it was observed that increasing the number of microchannels reduces thermal resistance due to the greater surface area for heat transfer. However, a higher number of channels also results in increased pressure drop. Therefore, finding an optimal channel number is dependant on the available pumping power to minimize thermal resistance effectively. Advanced thermal coolants were also investigated in heat sinks to improve their thermal performance. In this effort, Sajid et al. [8] investigated the potential of nanofluids containing titania nanoparticles suspended in water to improve heat transfer. It was observed that the nanofluids showed better heat transfer performance than distilled water in all tested wavy channel heat sinks, due to the higher thermal conductivity imparted by the titania nanoparticles. Their findings highlighted the significance of a balanced approach that considers both heat transfer enhancement and the associated pumping power for overall energy efficiency in cooling applications. Sheikholeslami and Ebrahimpour [9] conducted a study with the aim of improving the hydrothermal performance of Fresnel reflectors (FR) using innovative techniques. By employing computational fluid dynamics simulations, the researchers investigated the effects of introducing aluminium oxide nanoparticles into water to prepare the nanofluid coolant. The findings indicated that the suspension of nanoparticles yields a promising improvement of 0.15% in thermal efficiency of the FR solar system compared to using pure water as the coolant.

Sajjad et al. [10] experimentally investigated the thermal and exergetic performance of corrugated minichannel heat sinks using distilled water and nanofluid of magnesium oxide. Nanofluids showed enhanced heat transfer compared to distilled water, with higher nanoparticle concentration and Reynolds number leading to better performance. The heat sink with the smallest amplitude and wavelength exhibited the best thermal and exergetic efficiency, demonstrating the advantages of using MgO nanofluids in corrugated minichannel heat sink designs. The effects of channel configuration, nanoparticle concentration, Reynolds number, and heating power were examined on heat transfer and exergy efficiency. The results demonstrated that the heat sink with the smallest amplitude and wavelength exhibited better performance. Additionally,

nanoparticle loaded fluid showed enhanced heat transfer compared to distilled water, with higher nanoparticle concentration and Reynolds number leading to better Nusselt number.

Krishnan et al. [11] experimentally investigated the effect of heating area orientation on flow boiling heat transfer and pressure drop characteristics of water in microchannel heat sinks. The study tested five orientations - horizontal upward facing (HU), horizontal with heating area vertically aligned (HV), vertical with upflow (VUF), horizontal downward facing (HD), and vertical with downflow (VDF) - at volume flow rates of 50, 100 and 150 ml/min. The results showed that orientation had a negligible effect on heat transfer performance except for the VDF orientation. At a flow rate of 50 ml/min, the VDF orientation exhibited a 13% lower critical heat flux and a 30% lower outlet heat transfer coefficient compared to the HU orientation. This was attributed to the opposing buoyancy force in VDF causing severe flow reversal and premature critical heat flux. The total pressure drop was also highest for VDF compared to other orientations. However, the effect of VDF orientation was reduced at higher flow rates of 100 and 150 ml/min. The percentage reduction in critical heat flux decreased to 10.3% and 7.4% respectively. Among all the orientations tested, the VUF orientation showed the best performance with higher critical heat flux, lower pressure drop and minimal fluctuations. The buoyancy force aids bubble movement in the flow direction. The HD and HV orientations exhibited more fluctuations at low flow rates due to vapour stagnation and non-uniform two-phase distribution respectively. Xie et al. [12] numerically studied the impact of various parameters like channel width, height, wall thickness, bottom thickness, and inlet velocity on the thermal resistance and pressure drop of water-cooled MCHS. A 3D numerical model was employed to simulate the conjugate heat transfer and fluid flow within the minichannels. According to the results, pumping power increased linearly with channel height at a constant inlet velocity, but it decreased with channel width. These results highlight the complex relationship between the geometric parameters of the MCHS and its hydraulic performance.

Koshoridze et al. [13] presented a thermodynamic analysis exploring the creation of charged equilibrium nanobubbles on smooth hydrophobic surfaces (HS) in contact with water. The change in Gibbs free energy with bubble formation was calculated, taking into account the surface energy, electrostatic double layer energy, and capillary effects based on the Kelvin equation. Their calculations divulged that the Gibbs energy plotted against bubble radius exhibits a minimum, suggesting the potential for spontaneous nanobubble generation. Moreover, they observed that higher water salinity and lower surface tension act as deterrents, reducing the likelihood of nanobubble formation. Pan and Yang [14] investigated the impact of surface hydrophobicity on the formation and stability of oxygen nanobubbles formed through solvent exchange. Nanobubbles are tiny gaseous domains that emerge on hydrophobic surfaces when a gas-saturated solution comes into contact with the hydrophobic surface. The findings indicated that hydrophobic particle surfaces facilitated more nanobubble formation compared to hydrophilic ones during solvent exchange. It was concluded that the hydrophobic surfaces stabilize nanobubbles for long times, while hydrophilic surfaces destabilize them, causing coalescence into microbubbles that quickly escape the solution. Yang et al. [15] focused on investigating the occurrence of nanobubbles at solid-water interfaces. They utilized tapping mode atomic force microscopy (TMAFM) to study silicon oxide wafer surfaces with varying degrees of nanoscale roughness and hydrophobicity. It was observed that no nanobubbles formed on smooth, hydrophilic silicon oxide surfaces immersed in gas-supersaturated solutions, and similarly, smooth dehydroxylated silicon oxide surfaces with intermediate hydrophobicity did not exhibit nanobubble formation. However, when the silicon oxide surfaces were methylated to make them more hydrophobic, nanobubbles did form randomly across the surface. Interestingly, the nanobubbles that formed on rough methylated surfaces were larger and more sparsely distributed compared to those on smooth methylated surfaces. Consecutive TMAFM imaging over time allowed the researchers to observe processes of nanobubble coalescence and disappearance, confirming their gaseous nature.

The surface hydrophobicity of heat sinks has been widely studied for its potential positive impact on performance by reducing pressure drop. However, several complications and issues need to be carefully considered before implementing hydrophobic surfaces in cooling applications. The presented study focused on observing critical factors by comparing a conventional surface with a hydrophobic surface (HS) in a straight-channel heat sink. Additionally, the study involved to investigate the effectiveness of a straight channel heat sink when dealing with high heat generating components that produce heat levels up to 250 W. The goal is to assess how well the heat sink performs in dissipating the significant amount of heat generated by such components and to evaluate its overall cooling efficiency under these challenging conditions. The findings shed light on one such issue that could impede the widespread adoption of hydrophobic surfaces, indicating the need for more attention from the scientific community.

According to the Scopus database, there is a substantial body of research focused on heat sinks, with approximately 21,205 documents available on the topic, as illustrated in Fig. 1. However, when we specifically filtered the results to include only studies related to "hydrophobic" surfaces in conjunction with heat sinks, the number of documents significantly reduced to a mere 57. The continued refinement of the results, specifically for the cooling or thermal management application revealed a limited number of studies, with only 26 documents found. In the existing literature, it is noteworthy that a majority of the studies concerning hydrophobic surfaces in heat sinks are predominantly numerical investigations, relying on simulations and theoretical models. This striking contrast highlights a critical gap in the existing research landscape, signalling the need for more extensive exploration and attention from the scientific community. Additionally, the findings contribute to the advancement of heat sink design and optimization, supporting the development of more efficient and reliable cooling solutions for a wide range of applications [16,17].

2. Experimental setup description

The experimental setup, incorporating various measurement devices and temperature control mechanisms, allows for a thorough investigation of the thermal and hydraulic behaviour of the straight channel heat sink. The setup consisted of a storage tank with a temperature-controlled water bath, a gear pump, a needle valve, a flow measuring device, a pressure transducer, a heat sink assembly section with an integrated microscope camera, and a radiator, as depicted in Fig. 2.

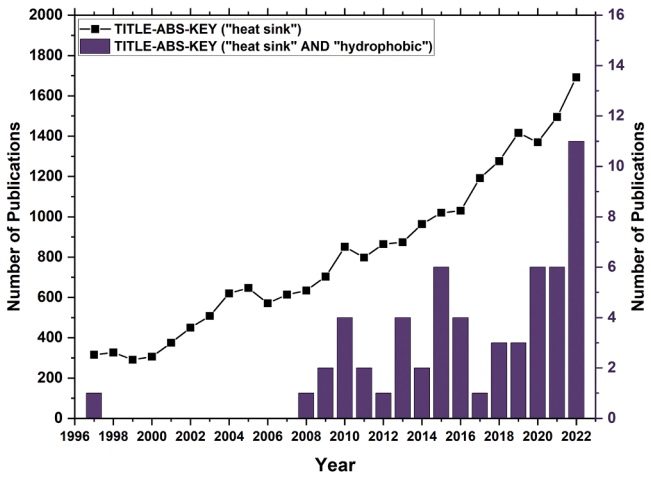

Fig. 1. Comparative Analysis of Research Publications on Heat Sinks over the past 25 years (Scopus database).

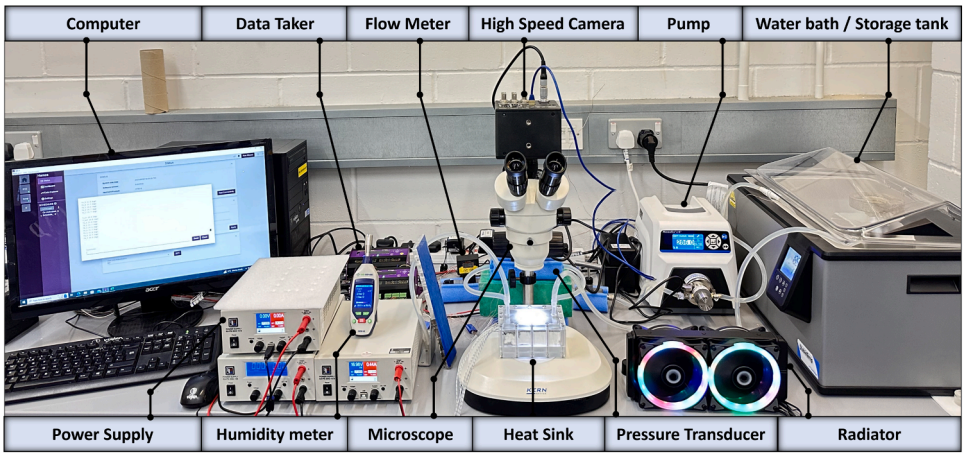

Fig. 2. Experimental test rig for accessing the thermal and hydraulic performance of heat sink.

To initiate the experimental cycle, coolant was pumped from the storage tank using a Masterflex gear pump (GJ-N23-PF1SA, UK). The flow rate was regulated by a flow control valve interconnected in between the pump and flow meter. To measure the rate of circulating fluid, a precise flow measuring device (Omega FTB332D-PVDF, USA) was installed just before the section under investigation. A heat sink insulated properly with wool surrounded by acrylic plates assembly was placed on the microscope base (KERN OZM-5, Germany). To analyse the flow and formation of bubbles a high speed came was installed on the top via camera adaptor connector. To maintain a constant heat flux, three cartridge heaters (RS-860–6845, UK) were inserted within the heat sink, with the desired power supplied by a DC power supply. The pressure drop across the heat sink was accurately measured using a pressure transducer (Omega PX2300, USA) connected across the heat sink having ends connected with the inlet and outlet.

The coolant continuously flowed through the heat sink channels, carrying the heat generated by the heaters. To evaluate the wall temperature, seven k-type thermocouples (RS-397–1589, UK) were strategically positioned at the base along the length of heat sink channels, below the wall surface. In addition, one thermocouple was placed at the inlet and another at the outlet of the heat sink to record the respective temperature values. The fluid, carrying the heat from the sink, passed

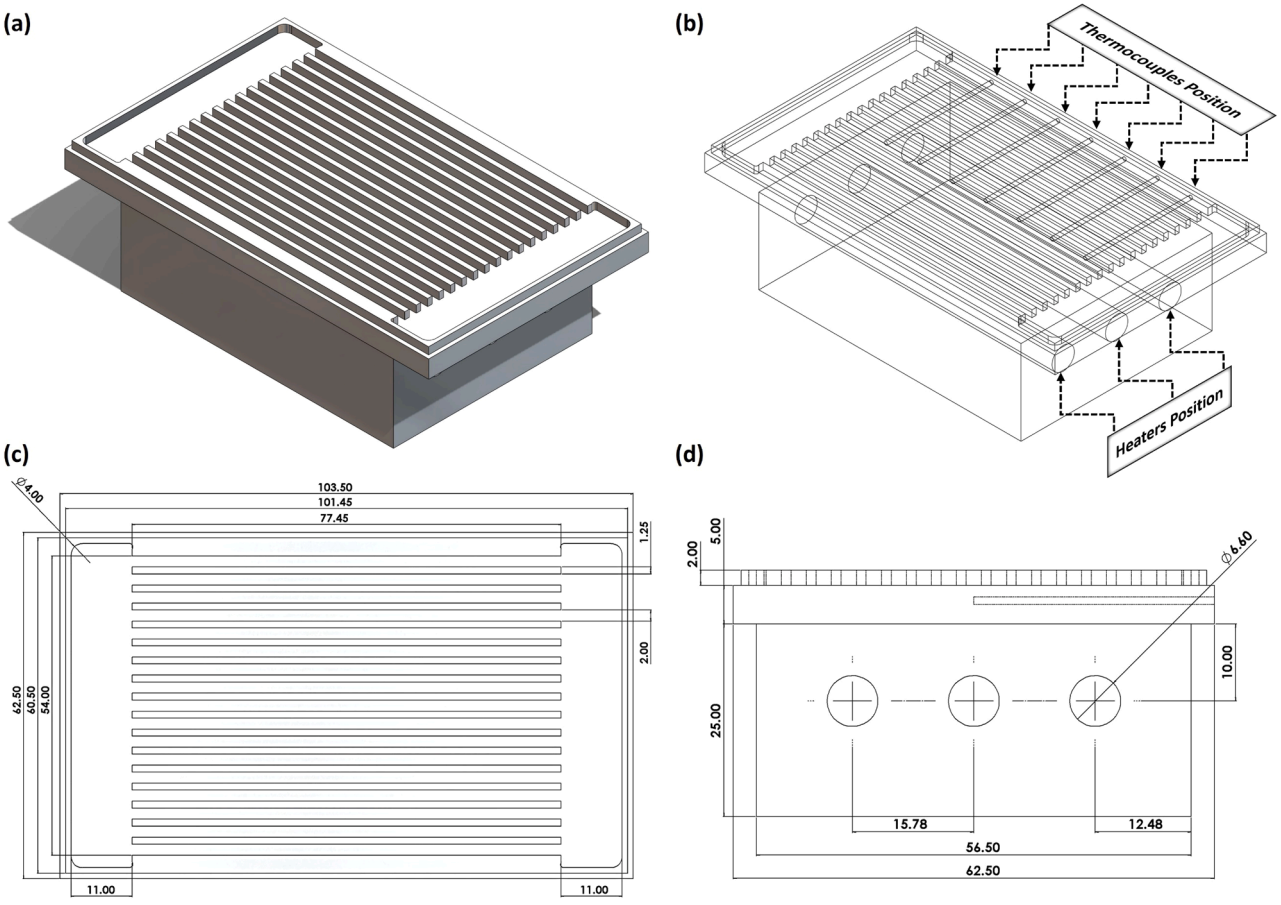

Fig. 3. Geometrical configuration of the heat sink, illustrating the dimensional parameters and positions of heaters and thermocouples.

through a radiator attached just after the heat sink to dissipate the heat to the surrounding atmosphere. Finally, the working fluid completed the loop by transferring back into the storage tank.

Fig. 3 presents the geometrical configuration of heat sink from different perspectives: an isometric, side, and top view, along with a comprehensive description of its design and the placement of heaters and thermocouples. To ensure the heat sink's accuracy and appropriate size, it was manufactured using CNC machining. One of the considerations in the design process was the spacing between the fins. It was considered that a minimum of 1 mm tool bit could be used during production without incurring significant cost penalties and practical constraints. The choice of fin spacing was crucial because a more compact arrangement would require increased pumping power for effective heat dissipation. By allowing sufficient space between the fins, the heat sink can maintain efficient cooling performance without excessively taxing the system's power requirements. Aluminium was chosen over other materials like copper, silver, etc. to fabricate the heat sink due to its high thermal conductivity value, lightweight nature, and cost-effectiveness, making it suitable for various applications in electronics and industries where efficient heat dissipation is essential. The material is also ideal due to its corrosion resistance, ease of fabrication, and recyclability.

The dimensions of the heat sink can be customized based on the specific design and requirements of the system in which it will be used. In the present study, the heat sink's effective area was determined to be 77.45 mm x 56.5 mm, which matches the dimensions of Intel Xeon processors. This sizing decision ensures compatibility and optimal heat transfer between the heat sink and the processors. Furthermore, the power range considered in the study was specifically chosen to align with the power generated by processors belonging to the Xeon family. This selection allows for accurate assessment and evaluation of the heat sink's performance under realistic operating conditions. Fig. 4 displays the manufactured heat sink and its assembly, along with the deionized water that was purchased from Sigma-Aldrich and utilized as a coolant during this experimental study.

Different types of liquid suspensions and coatings have been employed to make the surface hydrophobic like fluoropolymers, silicones, hydrophobic nanocoating's, graphene, hydrophobic oils, etc. [18–20]. Espanhol-Soares et al. [21] used the sol-gel technique to apply the silica-based coating for making cotton fabrics superhydrophobic. The coating solution was applied to the cotton fabric using a spray technique. The fabric was hung vertically, and the solution was sprayed on the surface from 15 cm. This allows the solution to form a fine mist and coat the fabric evenly. The spray deposition of the sol-gel solution is a simple, scalable, and economical method for applying superhydrophobic coatings, as it requires minimal coating solution and no complex equipment, unlike dipping or soaking techniques. Ogihara et al. [22] employed the silica nanoparticles suspended fluid spray to make paper water repellent while maintaining its transparency. The method involves pre-treating commercially available silica nanoparticles of around 25 nm size to make them hydrophobic by attaching dodecyl groups to their surface. These nanoparticles are then suspended in alcohol like 1-propanol, ethanol, or 1-butanol. A glass vaporizer was used to spray a nanoparticle suspension onto paper substrates. To achieve the desired coating amount, the spraying process was repeated multiple times. The simple spraying technique allows the creation of transparent and superhydrophobic coatings on paper using commercially available hydrophobic silica nanoparticles suspended in alcohols like ethanol. In the presented study, 303 graphene nanospray coating was applied in a scientifically appropriate manner following the directions of the supplier. The nanospray offers a range of benefits, including improved hydrophobicity, durability, and resistance to scratches and stains. When applied to a substrate, such as a heat sink, it forms a protective layer that repels water, helps reducing the risk of corrosion, and enhanced lifespan of the coated surface. The process began with thorough surface preparation, where the heat sink surface was meticulously cleaned and dried to achieve optimal cleanliness and eliminate any potential contaminants. Subsequently, a microfiber or foam applicator was selected to spray the graphene nanospray onto and then rub it on the surface in a crisscross pattern. This method ensured precise control and even distribution of the coating across the surface of the heat sink. One notable advantage of this particular coating was its immediate usability. Unlike other coatings that require additional curing time, the 303 graphene nanospray coating did not require any waiting period. Additionally, the supplier asserted that the coating could withstand for a period of twelve months.

Following the application, the coating underwent a curing process, during which it formed a haze or white film on the surface. This haze indicated that the coating was properly curing and adhering to the heat sink. In the next step, a clean dry microfiber towel was used to gently buff off any excess or unbound coating from the surface. This step was crucial in achieving a smooth and uniform coating layer on the heat sink. The heat sink, once buffed, was ready to be introduced to water immediately.

By meticulously following this appropriate application process, the 303 graphene nanospray coating effectively provided a hydrophobic surface on the heat sink. To assess the effectiveness of the 303 Graphene nanospray coating in improving surface wettability, a wettability test was conducted. Before the application of the coating, the contact angle of water on the surface was measured to be 74°±2°degrees, as shown in Fig. 5. This angle indicates the degree to which water spreads or beads up on the surface.

After the application of the nanospray coating, another wettability test was performed, revealing a significant increase in the contact angle. The water angle was measured to be 100°±2° degrees that was above 90°, indicating a substantial improvement in surface hydrophobicity. The larger contact angle suggests that the coated surface repels water more effectively, preventing it from spreading and forming droplets instead. This observation demonstrates the efficacy of the 303 graphene nanospray in enhancing the hydrophobic properties of the surface.

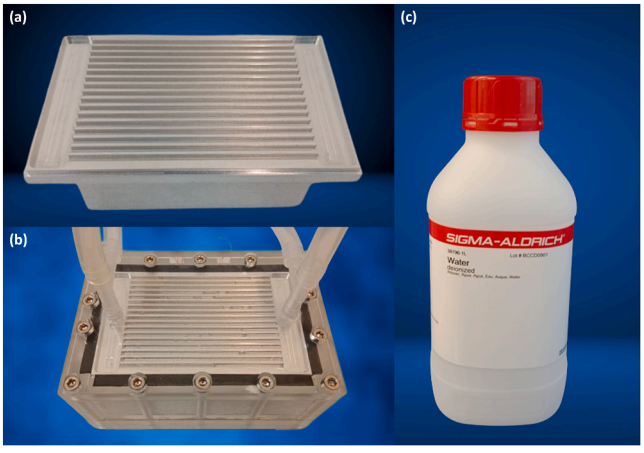

Fig. 4. (a) Manufactured heat sink, (b) heat sink assembly, and (c) coolant used during this study.

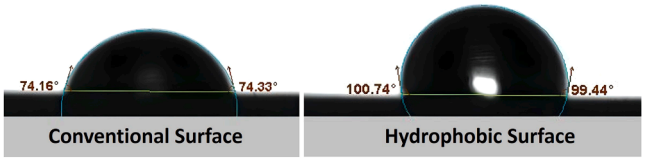

Fig. 5. Visual representation of the water contact angle during drop testing on both the conventional surface and hydrophobic surface.

3. Data processing

During the experimental campaign, data was collected at regular intervals to capture the thermal performance of the liquid-cooled heat sink. The measured data included the inlet and outlet temperatures of the working fluid, as well as the temperatures at specific positions within the heat sink. Additionally, parameters such as flow rate, pressure drop, and heat dissipation were recorded. To analyse the experimental results obtained from the experimental study, several equations and calculations were employed to determine various parameters related to heat transfer and thermal performance. These calculations helped quantify important factors such as thermal resistance, Reynolds number, Nusselt number, pressure drop, and wall temperature.

The hydraulic diameter is calculated based on the dimensions and geometry of the channel. For a straight channel heat sink with a rectangular cross-section, the hydraulic diameter (d_h) can be determined using Eq. (1) [23].

$$Hydraulic\ diameter\ (d_h) = \frac{4A}{P} \tag{1}$$

where A symbolized the cross-sectional area of the channel and P represented wetted perimeter of the channel. For rectangular channels, the A is calculated using Eq. (2), while P is computed with Eq. (3).

$$Cross\ sectional\ area\ (A) = height\ (h) \times width\ (w) \tag{2}$$

$$Wetted\ parameter\ (P) = 2\ \times [height\ (h) + width\ (w)] \tag{3}$$

The calculation of the heat transfer rate (Q) between the coolant flowing within the channels and the heat sink is performed using Eq. (4)

$$Q = mC_p(T_{outlet} - T_{inlet}) \tag{4}$$

where T_{inlet}, T_{outlet}, m, and C_p denoted the inlet temperature, outlet temperature, mass flow rate, and heat capacity respectively.

Temperature measurements were taken using thermocouples positioned just below the channel wall (T_b). The channel wall temperature (T_w) was computed using Eq (5), which relates it to the heat transfer rate (Q), distance from base to channel wall (l_x), thermal conductivity of heat sink (k_s), and the surface area of the channel wall (A_w), however, Eq. (6) was employed to determine A_w.

$$T_w = T_b - \left(\frac{Ql_x}{k_s A_w}\right) \tag{5}$$

$$A_w = L_s \times W_s \tag{6}$$

L_s and W_s denoted the width and length, respectively, of the specific section of the heat sink that is under consideration.

The logarithmic mean temperature difference ($LMTD$) was evaluated with Eq. (7), while Eq. (8) was used to determine the convective heat transfer coefficient (h_{conv}) [24].

$$LMTD = \frac{(T_w - T_{inlet}) - (T_w - T_{outlet})}{\ln\left[\frac{(T_w - T_{inlet})}{(T_w - T_{outlet})}\right]} \tag{7}$$

$$h_{conv} = \left[\frac{mC_p(T_{outlet} - T_{inlet})}{A_{eff} \times (LMTD)}\right] \tag{8}$$

where A_{eff} is the effective surface area of the channels, which represents the area in contact with the flowing fluid, was calculated using Eq. (9).

$$A_{eff} = [wL_s + 2(hL_s)]\ t \tag{9}$$

t symbolized the number of channels.

The Reynolds number (Re) was calculated to characterize the flow regime inside the heat sink channels. Eq. (10) was employed to determine the Reynolds number, which takes into account the fluid properties such as density (ρ), velocity (v), and viscosity (μ).

$$Re = \frac{\rho v d_h}{\mu} \tag{10}$$

The average fluid velocity was computed by dividing the volumetric flow rate (V) of the coolant by the cross-sectional area of the channel. This calculation provides an indication of the average speed at which the coolant flows through the channel, Eq. (11).

$$v = V/A \tag{11}$$

The resistance to heat flow, thermal resistance (R_{th}) was determined using Eq. (12), while the dimensionless parameter Nusselt Number (Nu) was calculated using Eq. (13).

$$R_{th} = \frac{LMTD}{Q} \tag{12}$$

$$Nu = \frac{h_{conv} d_h}{k_f} \tag{13}$$

where k_f denoted the fluid thermal conductivity.

The results obtained from these computations were then analysed to draw conclusions about the performance of the under investigation heat sink using water as the working fluid.

In micro or mini scale experiments, uncertainty analysis plays a crucial role in accurately demonstrating the experimental results and carefully examining the errors associated with measuring instruments. To determine the uncertainties in various measuring parameters, the study utilized a technique consistent with that employed by various other investigators. This approach ensures a comprehensive understanding of the experimental data and helps to enhance the reliability and precision of the findings. the study determined the uncertainties in different parameters, applying the set of Eq. (14-18). The results indicate that the maximum values of uncertainty for hydraulic diameter, Reynolds Number, and Nusselt number were found to be below or equal to 1.41%, 6.18%, and 6.26%, respectively. However, Table 1 presents the values of accuracy associated with the various instruments used in the study.

$$\frac{U_{d_h}}{d_h} = \sqrt{\left(\frac{U_h}{h}\right)^2 + \left(\frac{U_w}{w}\right)^2} \tag{14}$$

$$\frac{U_v}{v} = \sqrt{\left(\frac{U_{d_h}}{d_h}\right)^2 + \left(\frac{U_m}{m}\right)^2 + \left(\frac{U_A}{A}\right)^2} \tag{15}$$

$$\frac{U_{Re}}{Re} = \sqrt{\left(\frac{U_\rho}{\rho}\right)^2 + \left(\frac{U_v}{v}\right)^2 + \left(\frac{U_\mu}{\mu}\right)^2} \tag{16}$$

Table 1
Measuring Instruments range and accuracy.

Instrument	Range	Accuracy
Flow meter	0.1 – 1 l/min	± 6%
Thermocouple	−75 – 260 °C	± 1.5 °C
Pressure Transducer	0 – 1 psid	± 0.25%
Power Supply	0 – 84 V	Voltage < 0.2%
	0 – 10 A	Current < 0.3%

$$\frac{U_h}{h} = \sqrt{\left(\frac{U_m}{m}\right)^2 + \left(\frac{U_{(T_w - T_i)}}{(T_w - T_i)}\right)^2 + \left(\frac{U_{(T_w - T_o)}}{(T_w - T_o)}\right)^2 + \left(\frac{U_{C_p}}{C_p}\right)^2 + \left(\frac{U_{A_{eff}}}{A_{eff}}\right)^2 + \left(\frac{U_{(T_{out} - T_{in})}}{(T_{out} - T_{in})}\right)^2} \tag{17}$$

$$\frac{U_{Nu}}{Nu} = \sqrt{\left(\frac{U_h}{h}\right)^2 + \left(\frac{U_{d_h}}{d_h}\right)^2 + \left(\frac{U_{k_f}}{k_f}\right)^2} \tag{18}$$

4. Results and discussion

4.1. Validation

The validation of the experimental test rig was conducted by comparing the obtained results with the classical model developed by Shah et al. [25]. This model is widely used for predicting the Nusselt number in laminar flows under constant heat flux boundary conditions, as represented by Eq. (19). Numerous studies in the literature have employed the Shah model to validate their experimental findings, emphasizing its applicability across various research scenarios [26–29]. To assess the deviation between the experimental results and the values predicted using the Shah model, we employed the mean absolute error (MAE) [30,31], as depicted in Eq. (20). The MAE provides a measure of the average magnitude of the differences between the experimental and predicted values. By calculating the MAE, researchers can gauge the level of agreement between the experimental and predicted values. According to the results, the MAE was found to be consistently less than 5%, indicating a good agreement between the experimental data and the predictions made by the Shah model, as shown in Fig. 6.

$$Nu = \begin{cases} 1.953\left(Re\ Pr\frac{d_h}{l}\right)^{1/3} & if\left(Re\ Pr\frac{d_h}{l}\right) \geq 33.3 \\ 4.364 + 0.0722\left(Re\ Pr\frac{d_h}{l}\right) & if\left(Re\ Pr\frac{d_h}{l}\right) < 33.3 \end{cases} \tag{19}$$

$$\text{Mean Absolute Error (MAE)} = \frac{1}{n}\sum_{j=1}^{n}\left[\frac{\left|x_{exp.} - x_{pred.}\right|}{x_{exp.}}\right] \times 100\% \tag{20}$$

The equation involves the symbols l, Pr, d_h, n, $x_{exp.}$, *and* $x_{pred.}$, which respectively represent the finned section length, Prandtl number, hydraulic diameter, number of data points, experimental values, and predicted values respectively.

Additionally, to ensure the comprehensiveness of our analysis, the results were also compared with other models proposed by different researchers. Liu et al. [30] performed a series of experiments on a copper heat sink with square-shaped pin-fins, covering a range of Reynolds numbers from 60 to 800. The arrangement of the fins on the surface offered an interrupted passage to the flowing water, which effectively disrupted the flow and promoted better mixing and turbulence. The findings demonstrated that heat dissipation improved with increasing flow rate and surface temperature. Moreover, the researchers developed a model based on the experimental data to predict Nusselt number values for single-phase flow, represented by Eq. (21). The data was also correlated with the values predicted using the model developed by Kosar et al. [32] while investigating the thermal characteristics of microscale heat sink made of an array of hydrofoil-shaped pin fins. The correlation represented with Eq. (22) was found to be reliable, as provided a close approximation to the experimental values with a MAE of 4.1% for the specific configuration of the fins. However, for the presented study, the model provided predictions with an acceptable error range, as indicated by a MAE of 7.64%. Azizi et al. [33] examined the cylindrical micro-channel heat sink employing water and the nanoparticles suspended fluid as a cooling agent. A new correlation was developed by modifying existing models to predict the Nusselt number, incorporating the effects of Reynolds number, Prandtl number, and nanoparticle volume fraction for the case of nanofluids. It was found that demonstrating a satisfactory agreement with the experimental data within a ± 10% error range. The simplified form of the developed model, which considers a particle loading of 0%, is expressed by Eq. (23).

$$Nu = 0.1245\ Re^{0.6106}\ Pr^{0.36}\ (Pr/Pr_s)^{0.25} \tag{21}$$

$$Nu = 0.238\ Re^{0.488}\ Pr^{1/3}\ (Pr/Pr_s)^{0.25} \tag{22}$$

$$Nu = 0.293\ Re^{0.485}\ Pr^{0.2} \tag{23}$$

In order to demonstrate the variation of results within an acceptable

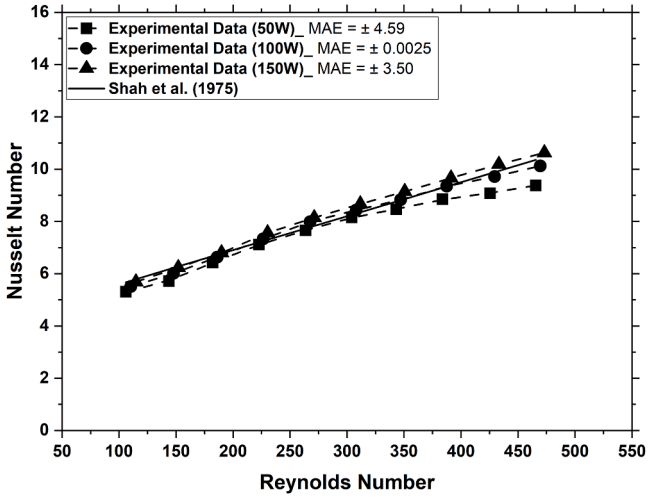

Fig. 6. Comparison of the experimental test results with the values predicted using the Shah correlation.

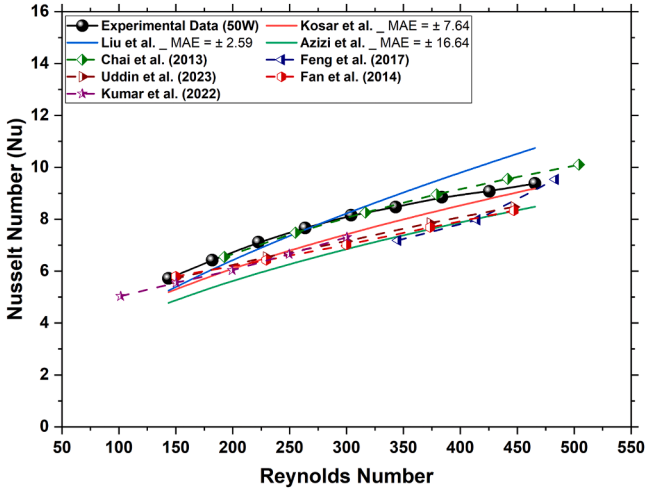

Fig. 7. Comparison of the test results with the predicted values of various models, as well as the results from experimental and numerical studies conducted by different authors.

range, investigators took into consideration several recent studies. By plotting the data points, Fig. 7 illustrates the range of variation observed amongst different experiments. This visualization allows us to assess the extent to which our results align with the broader body of experimental findings. Feng et al. [34] conducted a numerical study focusing on the analysis of rectangular microchannel heat sinks in laminar flow conditions, comparing plain channels with those incorporating wire coils. The investigation revealed noteworthy findings regarding pressure drop and heat transfer performance. It was observed that the plain channel exhibited the most favourable pressure drop characteristics amongst all configurations due to the absence of flow disturbances caused by the wire coils. However, the heat transfer performance of the plain channel was significantly lower than the wire coil configurations. Uddin and Sifat [35] examined and compared different designs of MCHS to evaluate their thermo-hydraulic performance. These designs include conventional straight channels as well as rectangular channels with straight, oblique, and a novel rounded secondary channel configurations in both parallel and counter flow arrangements. To ensure the accuracy of their findings, the numerical results were validated by comparing them with experimental and simulation data from previous studies, which showed good agreement. The results revealed that in parallel flow configurations, the secondary channels were found to have a minimal impact on heat transfer when compared to the conventional heat sink design. However, in counter flow configurations, all secondary channel designs demonstrate improved heat transfer performance, characterized by higher Nusselt numbers and lower thermal resistances. Kumar et al. [36] carried out a study that combined numerical simulations and experimental investigations to analyse the hydrothermal characteristics of straight and branched wavy channel heat sinks. Both configurations were designed to have identical hydraulic diameters (0.75 mm) and footprint sizes. The primary mode of heat transfer in these heat sinks occurs through convection between the channel walls and the fluid. However, it was observed that the heat transfer coefficient decreases along the channel as the thermal boundary layer thickens, leading to a reduction in the convection heat transfer rate. Additionally, the velocity and temperature fields within the streamwise direction are found to be relatively uniform in the straight channel heat sink (SCHS) microchannel, as there is minimal fluid mixing or flow disruption. Chai et al. [37] present a numerical investigation focusing on fluid flow and heat transfer characteristics within an interrupted microchannel heat sink, featuring rectangular ribs in transverse microchambers. The study systematically explored the effects of rib width, length, position, and microchamber spacing on heat transfer and pressure drop. The findings indicate that increasing the rib width enhances heat transfer; however, this improvement comes at the cost of increased pressure drop.

Fan et al. [38] conducted an investigation specifically focused on heat transfer and fluid flow characteristics within cylindrical oblique fin MCHS. The study employed computational fluid dynamics (CFD) simulations, with the aim of exploring the impact of varying parameters such as oblique angle, Reynolds Number, and secondary channel gap on the system. By visualizing the flow patterns, the researchers were able to observe how these parameters influenced the mixing and recirculation

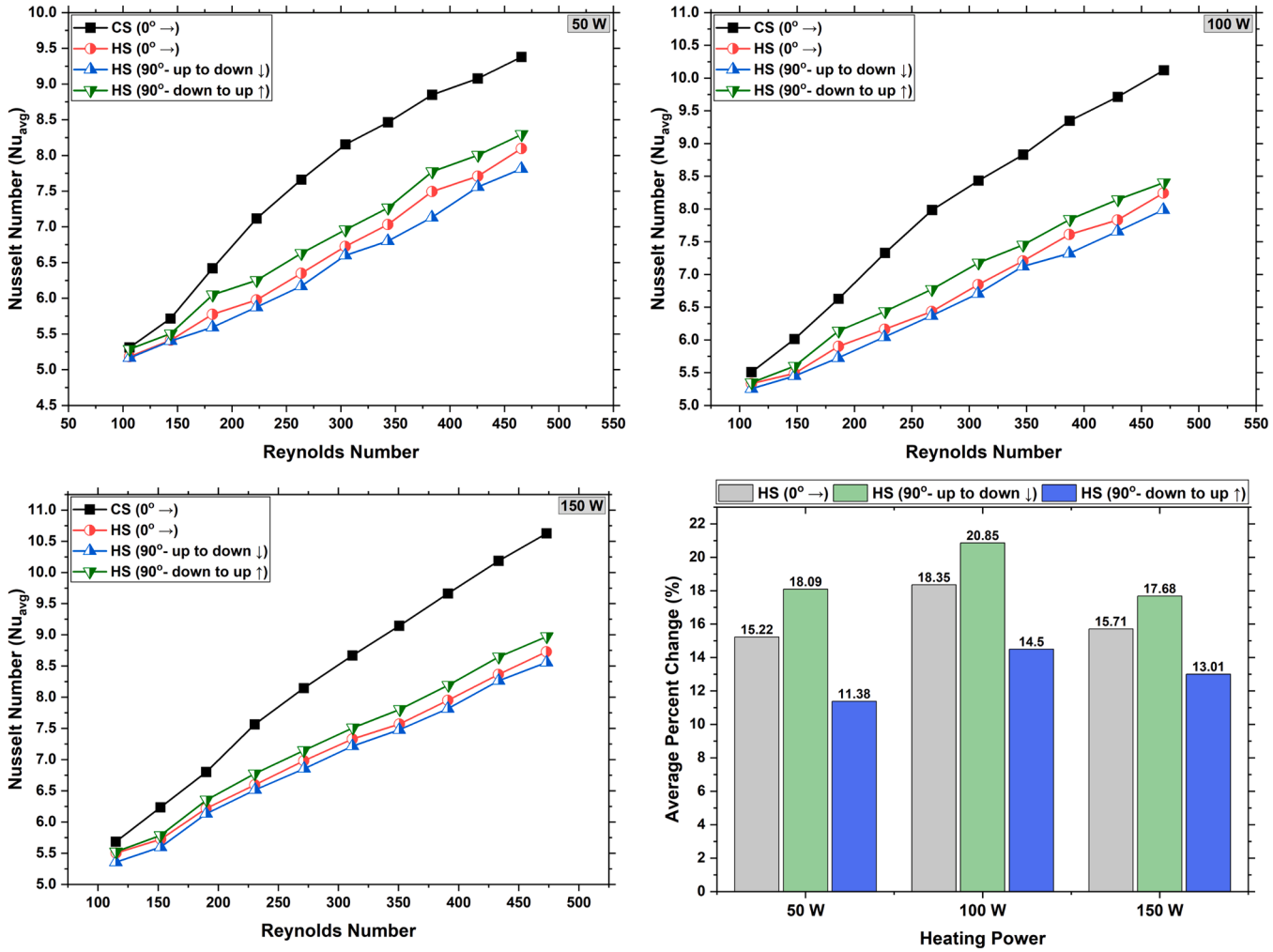

Fig. 8. Nusselt number variation of all studied configurations and conditions plotted against the Reynolds number at different heating powers.

of the fluid within the channels. The findings indicated that these factors had a significant impact on the average Nusselt number, which serves as a crucial measure of convective heat transfer.

This comparison and evaluation process helps us determine the effectiveness and reliability of the experimental test rig and its agreement with the established theoretical model proposed by Shah. It allows us to assess any discrepancies and analyse the performance of the rig under different operating conditions.

4.2. Nusselt number

The Nusselt number is a dimensionless number that relates the convective heat transfer to the conductive heat transfer. It characterizes the efficiency of heat transfer from a solid surface to a fluid.

Fig. 8 presents the results of a study conducted on a straight-channel heat sink, comparing the heat transfer performance of different surfaces and flow configurations plotting Nusselt number against the Reynolds number at various heating powers. As anticipated, the Nusselt number increases with increasing Reynolds number, exhibiting enhanced heat transfer efficiency at higher flow rates. Furthermore, at a constant Reynolds number, the Nusselt number shows a positive correlation with heating power. This observation aligns with the expected increase in heat transfer as the energy input to the heat sink rises. The maximum Nusselt numbers achieved with the CS heat sink were 9.38, 10.12, and 10.63 at heating powers of 50 W, 100 W, and 150 W, respectively.

When the CS heat sink was coated with a hydrophobic material, this coating is intended to make the surface water-repellent, a decrease in the Nusselt number was observed. This reduction can be attributed to the formation and retention of bubbles on the surface, creating stagnant zones or dead zones that impede heat transfer. The presence of surface tension may contribute to bubble formation. Additionally, the hydrophobic coating itself hinders heat transfer, leading to decreased Nusselt number compared to the CS heat sink. As the flow rate increases, the size of certain bubbles decreases due to the combination of lower wall temperature and fluid force. These smaller bubbles also move along with the fluid as the flow rate further increased. As a result, the influence of bubbles diminishes slightly, leading to a marginal increase in the Nusselt number. Nonetheless, the presence of a hydrophobic coating still plays a role in the overall process.

Phan [39] conducted a comprehensive study that revealed a notable difference between the conventional wetted surfaces and hydrophobic surfaces. According to the results, on hydrophobic surfaces, bubbles were observed even at extremely low levels of heat flux, and once formed, they remained on the surfaces instead of detaching. As the heat flux increased, the size of the bubbles grew, but still stayed on the surface. This phenomenon is likely attributed to the influence of surface tension force. On hydrophobic surfaces, characterized by low wettability and a reduced affinity for water, the formation of bubbles is favoured even at low heat flux. However, due to their hydrophobic nature, these bubbles face difficulty in detaching from the surface.

Wang et al. [40] noticed that bubbles began to form on superhydrophobic sites once the wall temperature approached 41.5 °C. As the temperature continued to rise, the bubbles expanded across the coated region. It is speculated that on hydrophobic surfaces, these bubbles may emerge even earlier. Additionally, it was concluded that the effect could be mitigated by degassing the working fluid and surface. The formation of nanobubbles is greatly influenced by the level of hydrophobicity of the solid surface and the polarity of working fluid. To investigate and comprehend the creation and arrangement of nanobubbles on uniform surfaces with varying degrees of hydrophobicity, Agrawal [41] employed various types of surfaces as solid substrates. Interestingly, nanobubbles do not form on flat hydrophilic surfaces when submerged in water but emerged spontaneously at the boundary between water and sleek, hydrophobic surfaces.

Bubbles can form on hydrophobic surfaces even at low temperatures like 30 °C [42], primarily due to the repulsion of water molecules and increased surface tension. This creates difficulties for air dissolution in water, resulting in the entrapment of small air pockets and subsequent bubble formation. In the case of our study, the surface was machined using a 1 mm drill tool bit, which introduced a certain level of surface roughness, creating localized variations in surface energy that could potentially facilitate the entrapment of air or gas pockets. It is noteworthy that bubble formation was not observed on the conventional surface before applying the hydrophobic coating. However, once the hydrophobic-coated surface comes into contact with the working fluid (water), the presence of these surface imperfections may contribute to promote the formation of bubbles [43]. This is primarily attributed to the influence of surface tension. The coating's hydrophobic properties, together with the roughness of the surface and the elevated surface tension, create circumstances that prevent air from dissolving in water, leading to the entrapment of small air or gas pockets and subsequent bubble formation.

When the hydrophobic-coated heat sink is placed vertically (90°) with the flow direction from bottom to top. The Nusselt numbers obtained were lower than that of the conventional surface heat sink but higher than the hydrophobic-coated heat sink in the horizontal position. This can be attributed to the movement of some bubbles with the flow, which carried heat and improved heat transfer to some extent.

Conversely, when the heat sink with the hydrophobic coating was positioned vertically with the flow direction from top to bottom. The heat transfer was lower in comparison to all other testing configurations including the conventional surface heat sink. In this particular configuration, the flow direction was opposite to the natural buoyancy-driven flow. The upward movement of bubbles counter to the downward flow direction could disrupt the convective heat transfer process, leading to a lower Nusselt number.

To compare the heat transfer performance of different heat sink configurations, the average reduction in Nusselt number is calculated as a percentage relative to the CS heat sink. It was found that the hydrophobic-coated heat sink in the vertical position with downward flow had the maximum reduction in Nusselt number values, followed by the coated heat sink in the horizontal position. The coated heat sink in the vertical position with upward flow showed the least reduction, indicating a slightly better performance due to the movement of bubbles with the flow.

The hydrophobic coated heat sink demonstrated reductions of 15.22%, 18.09%, and 11.38% in heat dissipation when operated at 50 W in horizontal, vertical downward flow, and vertical upward flow positions, respectively. As the power increased to 100 W, the formation of bubbles caused a noticeable increase in these values. However, at 150

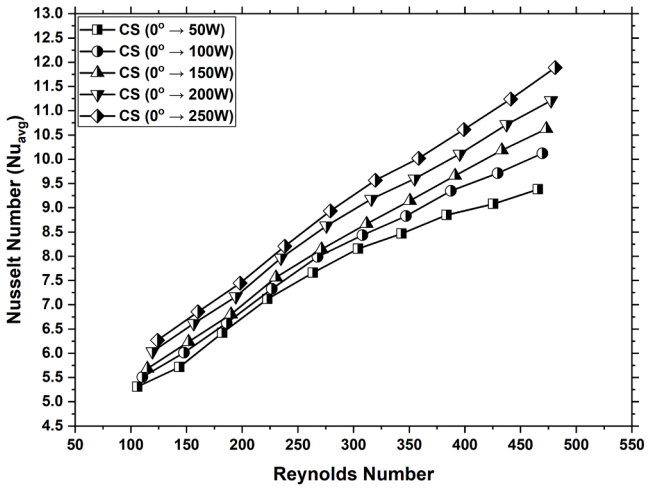

Fig. 9. Effect of varying Reynolds number and heating power on the Nusselt number of conventional surface heat sink.

W, even though more bubbles appeared on the surface, some of them became energized and moved with the flow, leading to a significant decrease in the reduction values once again, as shown in Fig. 8.

Furthermore, to address the heat dissipation challenges posed by high heat generating electronic components in various applications, the study was extended to analyse the conventional surface straight channel heat sink across a wider range of heating powers, from 50 W to 250 W. Notably, the analysis revealed a significant increase in the Nusselt number values as the heating power increased, Fig. 9.

A study was conducted to investigate the formation of bubbles on the surface of a heat sink under varying temperature and flow rate conditions. To capture the bubble formation, a microscope equipped with a camera was used. Initially, a tiny bubble was observed on the surface at 22.16 °C that formed and as anticipated stayed on the surface [13]. There was no noticeable increase in its size despite a considerable amount of time had passed. It was noticed that even a small amount of heat input can serve as a catalyst for bubble formation. However, when the temperature crossed the barrier of 26 °C a noticeable number of bubbles have been observed to appear on the surface. The numbers and size of some of the bubbles were observed to be increased with an increase in temperature up to 39 °C as depicted in Fig. 10a. The distribution of bubbles was found to be uneven across the channels. Specifically, a larger number of bubbles bigger in size were observed in the very left and right side channels. This uneven distribution could be attributed to variations in fluid flow and local conditions within the channels. In the second set of trials, the temperature was kept constant, increasing the flow rate from 250 ml/min to 860 ml/min, visualisation shown in Fig. 10b.

This approach could be effective in reducing the generation of bubbles either by preventing their formation or facilitating their movement

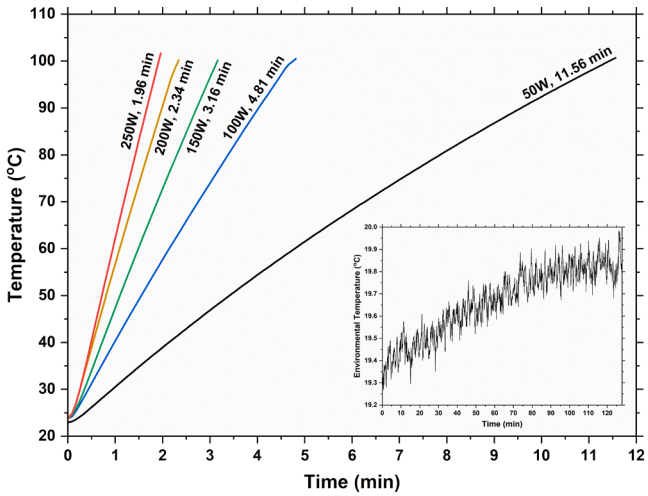

Fig. 11. Variation of heat sink wall temperature subjected to natural cooling conditions at different levels of heating power.

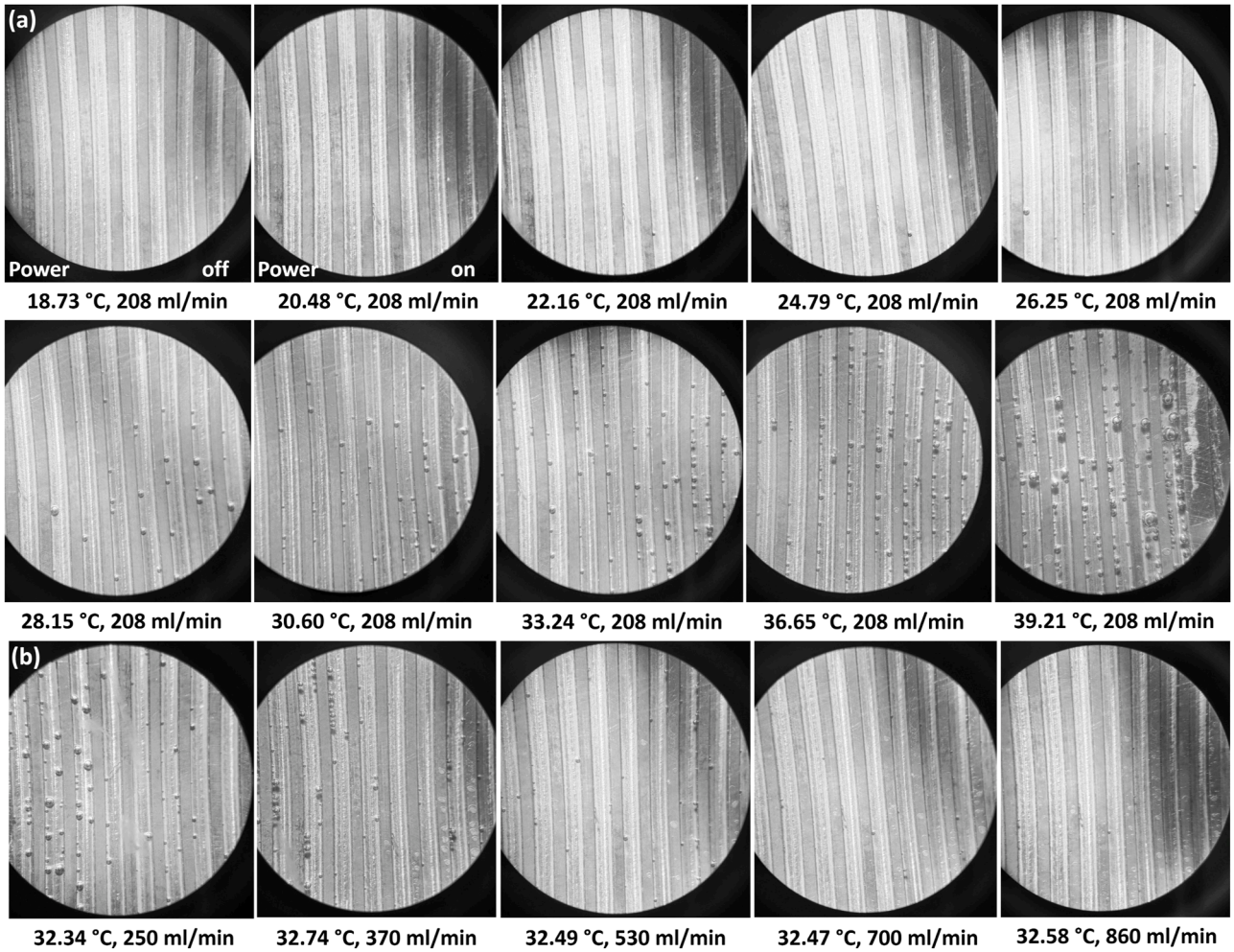

Fig. 10. Formation of bubbles within the hydrophobic channels under distinct experimental conditions (a) varying temperature keeping flow rate constant, (b) varying flow rate while restricting temperature.

in the direction of the flow. These findings highlight the complex dynamics of bubble formation and their behaviour for hydrophobic surfaces. It was revealed that the formation and movement of bubbles on the hydrophobic surface of the heat sink were directly influenced by the temperature and flow rate. However, further research and analysis to acquire a better grasp of the underlying mechanisms involved and to optimizing heat transfer performance, particularly in the presence of bubbles, which can significantly impact the overall efficiency of the system.

4.3. Wall temperature

The ability of a heat sink to effectively manage and regulate temperatures is vital for ensuring reliable and efficient operation in today's demanding environments. The variation of sink temperature was examined under natural cooling conditions, where the heat sink was placed in a room at ambient temperature. The study involved measuring the time it took for the temperature to reach 100 °C at various heating levels. It was observed that, at a power level of 50 W, it took approximately 11.56 min for the sink to reach a safe temperature. However, as the power level increased to 250 W, the time decreased to 1.96 min, as depicted in Fig. 11. These findings demonstrate the importance of cooling mechanisms, particularly liquid cooling, when dealing with high heat-generating components like those found in advanced technologies.

Traditional cooling methods may struggle to effectively remove heat in such scenarios, as evidenced by the rapid temperature rise observed in this experiment. Conversely, it was observed that circulating liquid coolant around the sink effectively absorbed and carried away the heat, consistently keeping the temperature below 55 °C even at the maximum applied heating power of 250 W.

As we move towards the future, emerging technologies such as AI continue to advance at a rapid pace. These advancements often result in the generation of substantial heat by the components involved. Failing to address this heat build-up can have severe consequences, including compromised performance and reliability. Therefore, investing in advanced cooling solutions becomes crucial. By implementing effective cooling mechanisms, we can ensure that these high-tech components operate optimally and avoid potential thermal damage.

Wall temperature is an essential parameter to consider when analysing the performance of heat sinks. The wall temperature of a heat sink refers to the temperature of its solid surfaces, particularly the surfaces in contact with the fluid or air that carries away the heat. The results of the study conducted on the straight-channel heat sink reveal important insights into the wall temperature variations under different test conditions. For all the testing configurations, a significant decrease in wall temperature was observed with an increase in flowrate, however, as anticipated the temperature values increase with heating power, as shown in Fig. 12.

The initial test was performed on the conventional surface (CS) heat sink, where the wall temperature was measured at different Reynolds numbers and heating powers. At a power of 50 W, the wall temperature exhibited a modest reduction from 25.952 °C to 22.171 °C as the

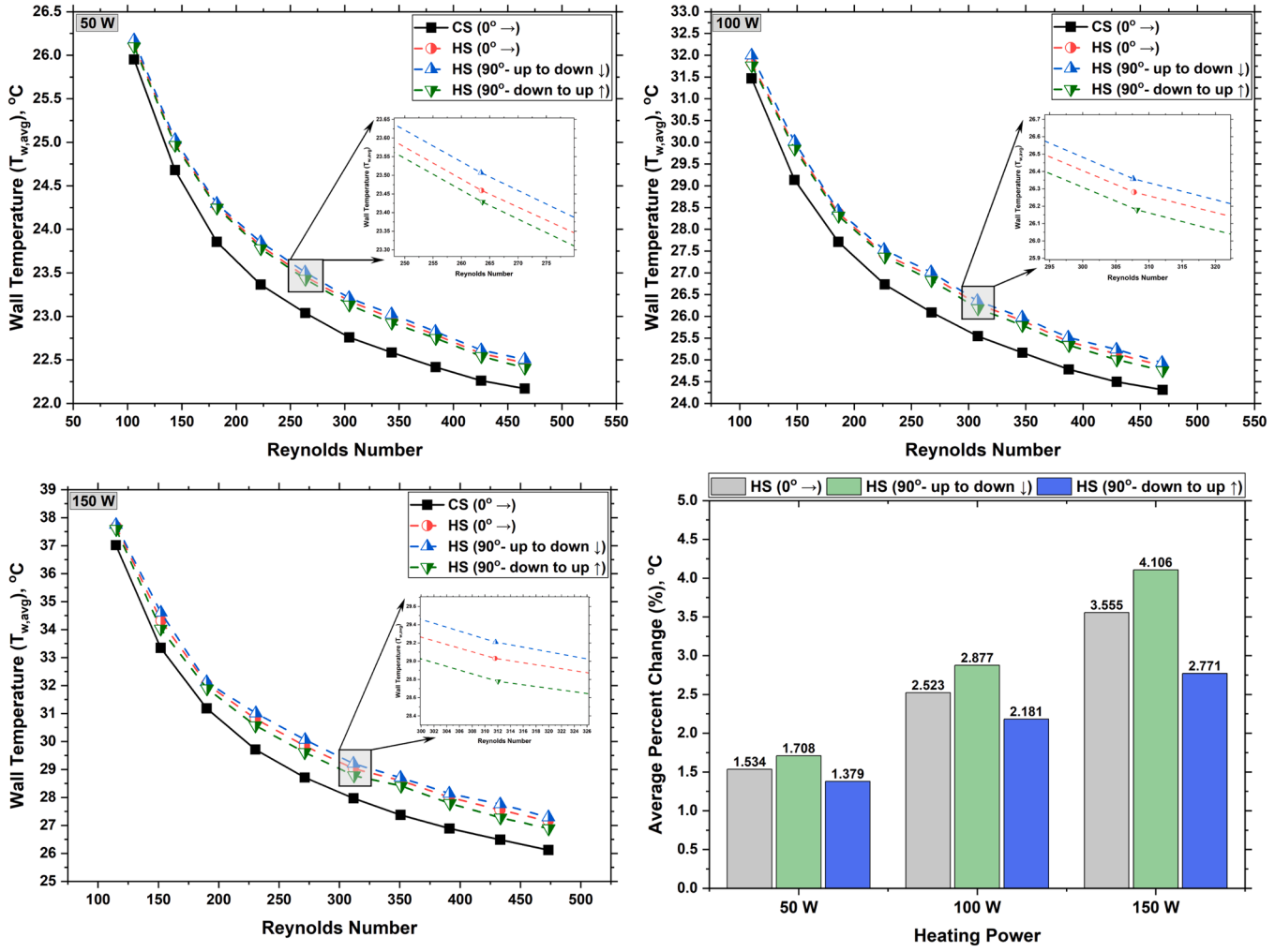

Fig. 12. Wall temperature variation across different configurations and conditions, plotted against Reynolds number at different heating powers.

Reynolds number increased. This suggests that there was effective heat dissipation. Additionally, at 100 W and 150 W, the wall temperature values decreased ranging from 24.31 °C to 31.47 °C and 26.12 °C to 37.02 °C demonstrating the ability of the CS heat sink to handle higher heat loads.

When a hydrophobic coating was applied to the heat sink in a horizontal position, an increase in wall temperature was observed across all heating powers. The wall temperature values at different Reynolds numbers and heating powers were slightly higher compared to the conventional surface heat sink. The increase in temperature can be attributed to the formation of bubbles on the surface inside the channels, creating a dead zone and reducing heat dissipation, as well as the contribution of the hydrophobic coating itself. The third test examined the hydrophobic coated heat sink in a vertical position with downward flow. This configuration showed higher wall temperatures compared to the CS and horizontally coated heat sinks. According to the results in comparison of CS, the average increase in wall temperature was 1.71% at 50 W, while it was 2.88% and 4.11% at 100 W and 150 W respectively. In the last test, the hydrophobic coated heat sink was positioned vertically with upward flow. The wall temperatures were relatively higher than the CS heat sink but lower than the vertically coated heat sink with upward flow. In this case, the highest wall temperature of 37.58 °C was observed at the highest testing heat power and the lowest flow rate.

Analysing the average increase in wall temperature percentages across the heating powers, it becomes evident that the coated heat sink in the vertical position with upward flow showed the minimum change compared to the other orientations. This suggests that the upward flow helps mitigate the negative effects of bubble formation to some extent.

In addition to the previous tests conducted on the conventional surface (CS) heat sink, the study was further extended to investigate its performance at higher heating powers of 200 W and 250 W, as illustrated in Fig. 13. The objective was to assess the heat sink's ability to effectively maintain the temperature of high heat-generating components in various application areas. Despite the increased heating power, the maximum value of average wall temperature observed in this study was around 46.62 °C. This outcome is significant and noteworthy, as it indicates the heat sink's capability to efficiently dissipate heat and effectively control the temperature even under demanding conditions.

The rise in heat sink wall temperature along its length as water flows through the channels was observed through the temperature variation that helps to analyse the thermal behaviour, as illustrated in Fig. 14. In order to capture these temperature changes, seven thermocouples were strategically installed along the heat sink's length, evenly spaced. The maximum variation in temperature along the channel was approximately 5.52 °C which indicates the extent of temperature fluctuations experienced along the heat sink.

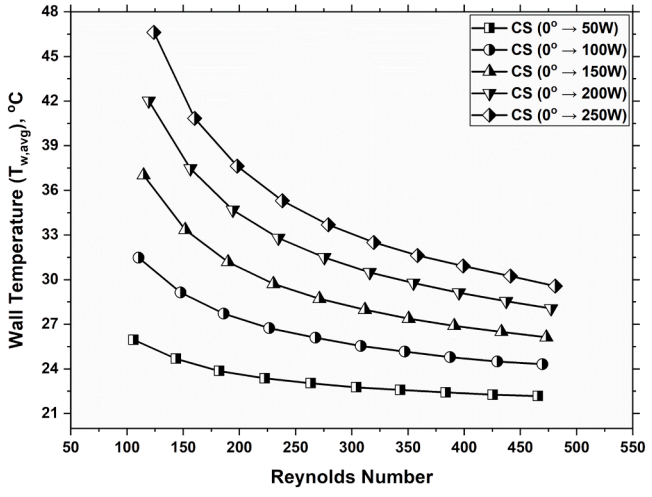

Fig. 13. Wall Temperature variation against the Reynolds number at different heating powers.

As anticipated, a consistent trend was observed across all testing conditions. There was a large temperature difference, as the water entered at a very low temperature compared to the heat sink which continuously generated a huge amount of heat, resulting in a greater amount of heat transfer. That is why the minimum value of wall temperature was observed at the leading end of the channels. A more gradual temperature rise is observed in the middle of the heat sink as the water progressed along the length. Moving towards the end, the temperature increase further slowed down, and a considerable fall in temperature was recorded near the trailing edge of the channels. In a numerical study conducted by Naqiuddin et al. [45] on a straight channel heat sink, a significant decrease in wall temperature near the trailing end of the channels was also observed. The formation of vortex and backflow at the trailing edge can contribute to the observed reduction in sink wall temperature near the end of the channels.

4.4. Thermal resistance

Thermal resistance is a crucial parameter in heat transfer analysis and characterizes the resistance to heat flow within a system. By minimizing thermal resistance, engineers can enhance heat transfer efficiency and maintain safe operating temperatures for electronic devices and other heat-generating systems. Thermal resistance in the case of liquid cooled heat sinks can be elaborated as the sink's effectiveness in transferring heat from a heat source to the flowing fluid.

In the study's results, the thermal resistance values were obtained for different heat sink configurations at varying flow rates and heating powers. As expected, the general trend of thermal resistance followed the inverse pattern of the Nusselt number. It exhibited a decrease in thermal resistance with increasing Reynolds numbers, indicating that higher flow rates enhance heat dissipation, as shown in Fig. 15. It was observed that the presence of the coating led to an increase in thermal resistance compared to the CS heat sink. Considering CS heat sink as the baseline, the maximum increase in thermal resistance value was observed to be 20.85% for surface treated vertically positioned heat sink and up to down flow direction. However, when the flow direction was reversed, a discernible reduction in thermal resistance was observed but still relatively higher compared to the CS heat sink. This indicates that while the upward flow direction improved the heat transfer performance to some extent, it was not as effective as the CS configuration. Overall, the average increase in thermal resistance compared to the CS heat sink ranges from 11.3% to 20.9% across the different heating powers and configurations. Higher heating powers 200 W and 250 W were also taken into consideration for this investigation, and it was found that the thermal resistance decreased even more as the heating power varied.

4.5. Pressure drop

The efficiency and performance of heat sinks are closely linked to their pressure drop characteristics. Pressure drop, or the resistance to fluid flow, plays a crucial role in determining the effectiveness of heat transfer within a heat sink. Understanding and analysing the variations in pressure drop across different heat sink configurations and operating conditions are essential for optimizing thermal management strategies. In this study, we examine the pressure drop behaviour of a straight-channel heat sink under different flow rates, heating powers, and surface conditions, the results revealed significant variations in pressure drop across different testing conditions.

The first set of tests was conducted on a CS heat sink, varying the flow rate and heating power. The observed data demonstrated a direct correlation between the Reynolds number and pressure drop, indicating that higher Reynolds numbers corresponded to increased pressure drops. The heat sink with a hydrophobic coating was examined to assess

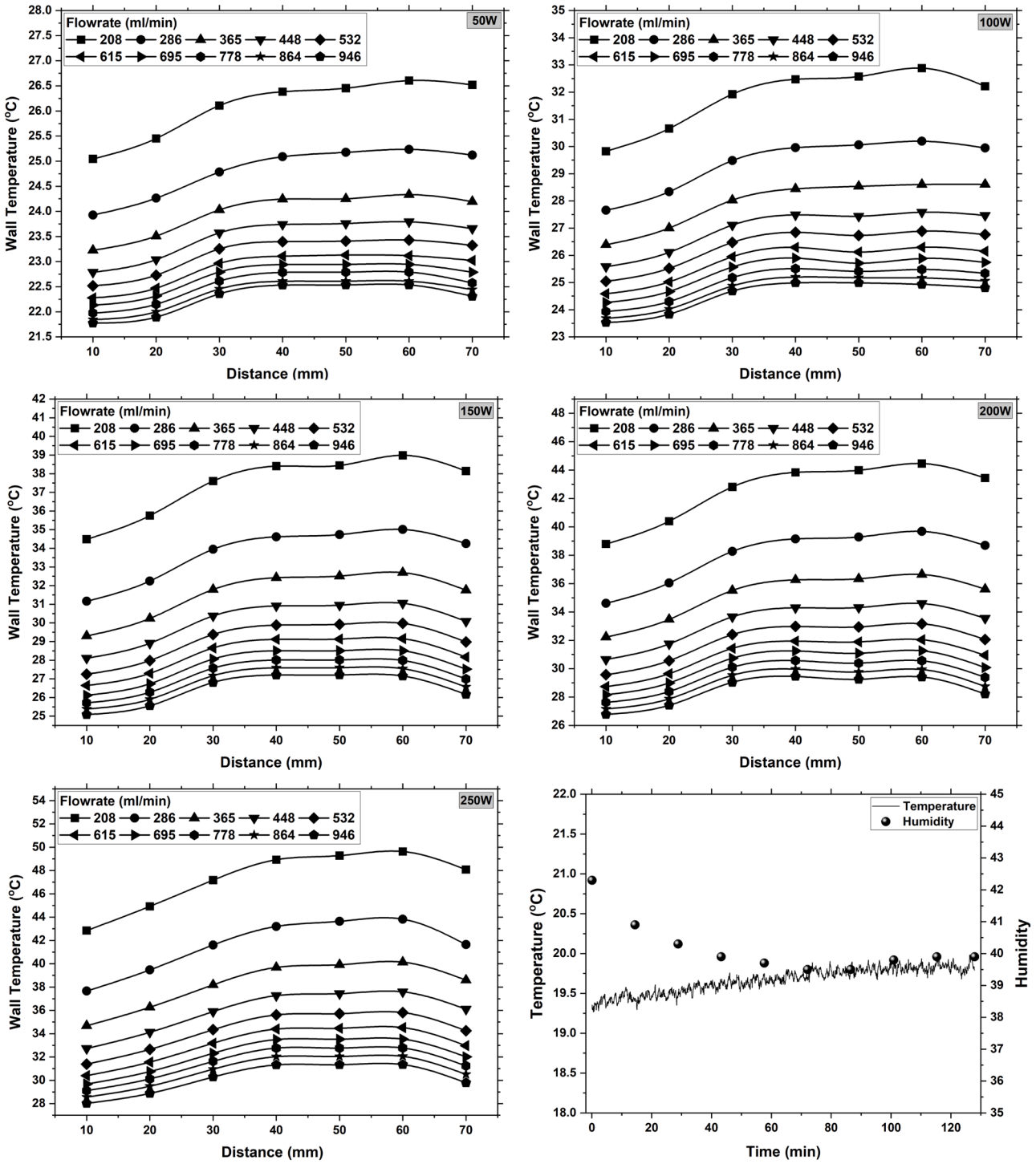

Fig. 14. Temperature variation along the length of a heat sink at different flow rates.

its impact on reducing the pressure drop. The results indicated a noticeable decrease in pressure drop compared to the conventional surface heat sink. However, this decrease was not significant due to the formation of bubbles at the lower flow rate values that hindered the fluid flow inside the channels. The presence of these bubbles limited the effectiveness of the hydrophobic coating in reducing the pressure drop. Initially, the pressure drop in the HS heat sink was found to be slightly higher compared to vertically positioned heat sinks. However, when the Reynolds number increased from 270 to 310, the higher flow rate effectively cleared the channels, leading to a subsequent decrease in pressure drop. Beyond this point, the horizontally positioned heat sink exhibited a lower pressure drop in comparison to the vertically positioned heat sink with upward flow, as illustrated in Fig. 16.

Interestingly, when the heat sink with the hydrophobic coating was positioned vertically with downward flow direction, the pressure drop was comparatively lower than both the conventional surface heat sink and the hydrophobic-coated heat sink in a horizontal and vertical position with flow direction down to upward. This observation suggests that gravity may have played a role in reducing the pressure drop. The downward flow direction, coupled with gravity, helps overcome the resistance caused by bubbles formed on the surface, resulting in a more efficient fluid flow. Finally, observed the heat sink with a hydrophobic

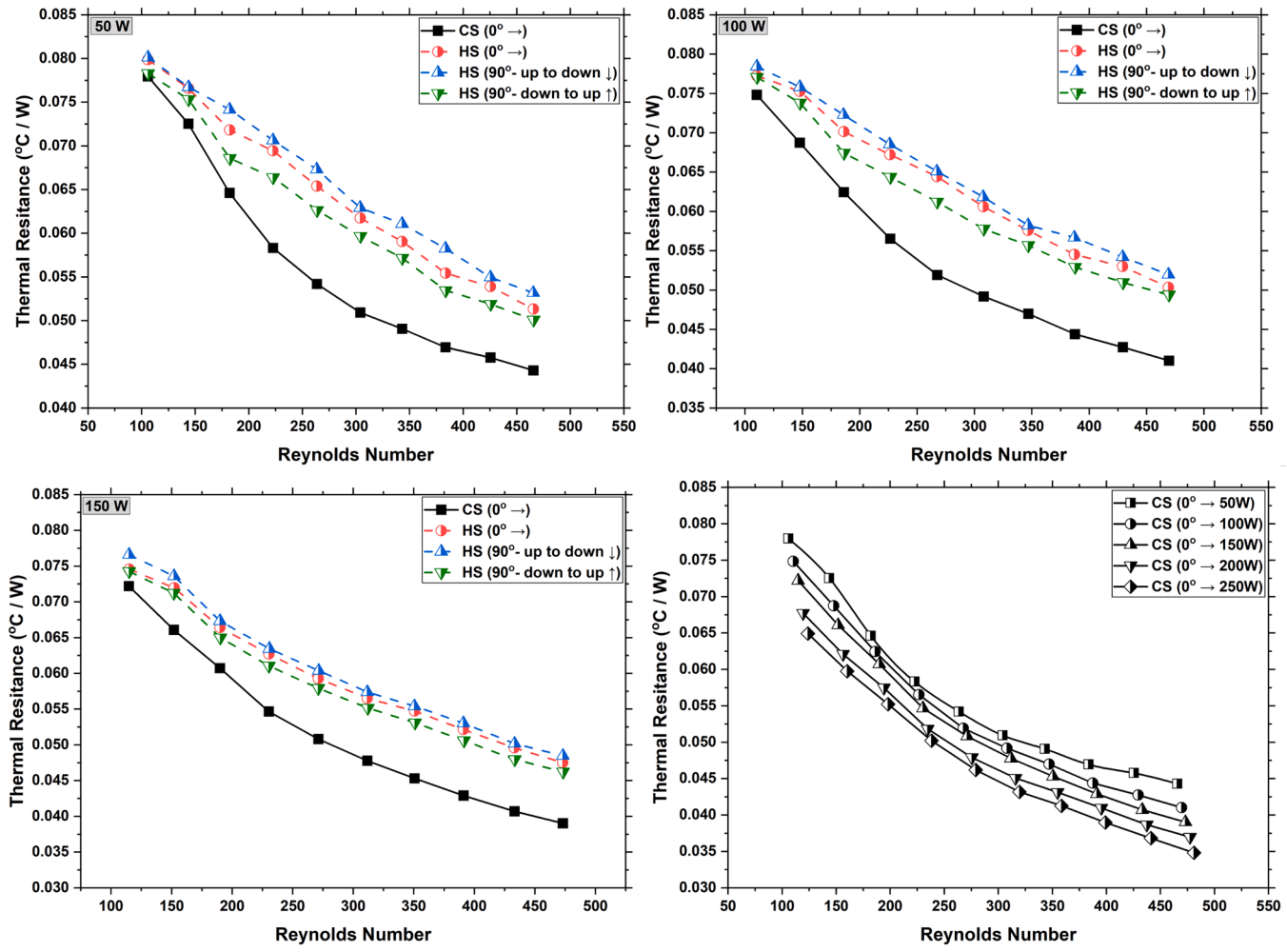

Fig. 15. Variation of thermal resistance with Reynolds number and heating power for studied configurations.

coating positioned but with the flow direction upward, from bottom to top. The observed pressure drop values were marginally higher than that of the vertically positioned heat sink with downward flow. Noticeably, in comparison to a horizontally positioned HS heat sink, at lower flow rate, the pressure drop was less due to the formation of bubbles. The results of this configuration showed that even though the flow direction was against gravity, some particles are carried along with the flow, reducing the overall resistance and resulting in a lower pressure drop compared to the horizontally positioned heat sinks. However, as the flow rate increased and the bubbles diminished, the pressure drop in the upward flow configuration surpassed that of the horizontal heat sink.

When comparing the average decrease in pressure drop across different heating powers and heat sink configurations with the conventional surface heat sink, some interesting trends emerged. The hydrophobic-coated heat sink in a vertical position with downward flow exhibited the highest average decrease in pressure drop across all heating powers. According to the results, at 50 W, the average decrease in pressure drop was noticed 11.92% relative to the CS heat sink. These findings shed light on the intricate interplay between fluid flow, sink orientation and bubble formation within the heat sink. Understanding these dynamics is crucial for optimizing heat sink performance. Further investigations into the underlying mechanisms governing these phenomena will deepen our comprehension and facilitate the design of more efficient heat sink systems.

In the extended part of this study, additional heating powers of 200 W and 250 W were applied to the conventional surface (CS) heat sink to investigate its impact on the pressure drop and the generation of bubbles. The results showed a decrease in pressure drop with increasing power input, as shown in Fig. 16, which is consistent with the behaviour observed in previous tests as no bubbles were observed on the surface of the CS heat sink despite the increase in heating power.

5. Conclusion

The presented study investigates the thermal and hydraulic performance of straight-channel heat sinks with different surface conditions and flow directions. The experimental investigation, coupled with detailed analysis and measurements, has provided a comprehensive understanding of the factors influencing heat transfer efficiency, wall temperature, and pressure drop characteristics in heat sink systems. Furthermore, the study brought attention to a potential challenge that may arise when employing hydrophobic surface heat sinks for cooling applications. The investigation revealed insights into the specific issues or limitations associated with the utilization of such surfaces, which could impact their overall cooling performance and efficiency. The acquired data has enabled us to draw several noteworthy conclusions of significant importance.

- The study demonstrated that the Nusselt number, which characterizes convective heat transfer efficiency, increases with higher Reynolds numbers and heating powers, indicating improved heat transfer at higher flow rates and energy inputs.
- Hydrophobic coatings on surfaces can lead to the formation and retention of bubbles due to the repulsion of water molecules,

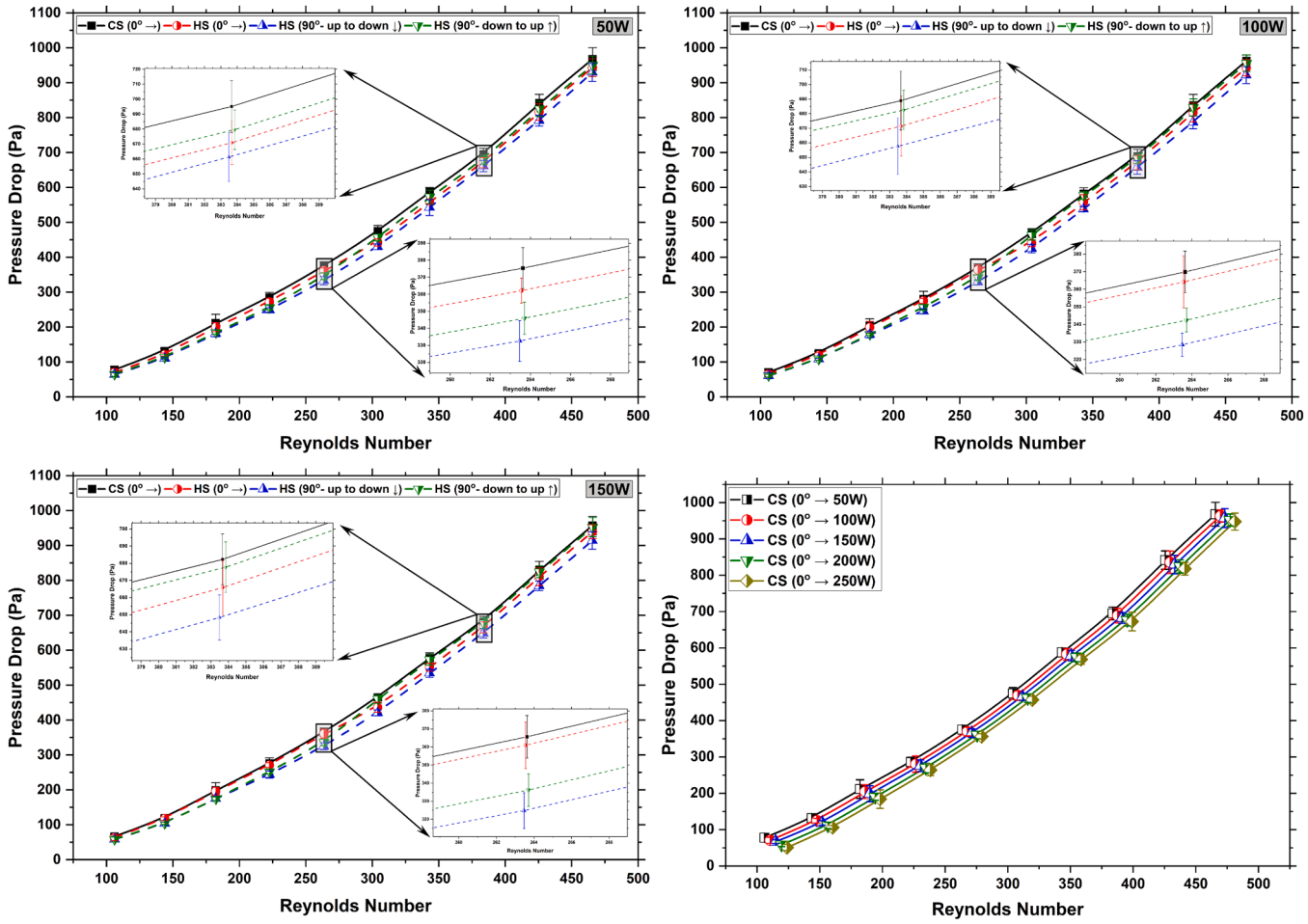

Fig. 16. Pressure drop variation across various heat sink configurations plotted against the Reynolds number at different heating powers.

increased surface tension, and localized variations in surface energy caused by surface roughness.

- The application of a hydrophobic coating to the heat sink surface reduced the Nusselt number due to the formation and retention of bubbles, as well as hindered heat transfer caused by the coating's hydrophobic properties. The orientation of the heat sink and flow direction also influenced heat transfer, with vertical downward flow showing the highest reduction in Nusselt number values. The hydrophobic coated heat sink exhibited reductions of 15.22%, 18.09%, and 11.38% in heat dissipation at 50 W, with increasing bubble formation correlating with power; however, at 150 W, certain bubbles became energized, leading to a subsequent decrease.
- The formation and behaviour of bubbles on the hydrophobic surface of a heat sink were directly influenced by temperature and flow rate. A considerable number of bubbles appeared on the surface when the temperature exceeded 26 °C and observed an increase in both the number and size as the temperature rose. Additionally, the distribution of bubbles across the channels was uneven, indicating variations in fluid flow and local conditions.
- The flow rate had a significant impact on bubble movement. Increasing the flow rate resulted in the bubbles moving in the direction of the flow, highlighting the strong correlation between temperature, flow rate, and bubble formation on the heat sink surface.
- The study observed a consistent trend in temperature variation along the length of the heat sink channels. As water flowed through the channels, a notable temperature disparity was evident, with the lowest wall temperature being recorded near the leading edge of the channels. The temperature gradually increased towards the middle of the heat sink and then the rate of increase slowed down as it approached the trailing edge. Near the trailing edge, a considerable fall in temperature was recorded, which could be attributed to the formation of vortex and backflow in that region.
- The presence of a hydrophobic coating on the heat sink surface led to a noticeable decrease in pressure drop compared to the conventional surface. However, at lower flow rate, the reduction in pressure drop was limited due to the formation of bubbles, which impeded fluid flow inside the channels. It was revealed that the hydrophobic-coated heat sink positioned vertically with downward flow exhibited the highest average decrease in pressure drop of 11.91% at 50 W compared to a conventional surface heat sink and all the other hydrophobic heat sink arrangements.
- The application of 303 graphene nanospray to create a hydrophobic surface displayed great promise in terms of hydrophobicity but also brought to light the complex interplay between hydrophobicity and heat transfer.
- While a hydrophobic coating may offer benefits such as enhanced surface protection and resistance to liquid damage, it introduces challenges in heat transfer performance. Hydrophobic coatings like 303 graphene nanospray may not be the ideal choice for applications prioritizing heat transfer improvement due to the trade-off between hydrophobicity and thermal characteristics. Nevertheless, they offer significant benefits in industries like automotive, building, and aerospace, where surface protection and heat loss reduction are of primary importance. In renewable energy, like solar panels and wind

turbines, these coatings could inadvertently impede heat dissipation, affecting overall efficiency.

- The findings suggest that achieving improved surface smoothness, optimizing flow conditions, incorporating effective anti-bubble additives, and thoroughly degasifying the coolant and system can significantly enhance surface repellence on hydrophobic surfaces. As a result, these measures effectively reduce the likelihood of bubble formation and entrapment while having minimal impact on the overall performance of the system.

Further research can explore alternative methods to mitigate bubble formation and improve heat transfer in hydrophobic-coated heat sinks. Investigating the impact of different surface materials, coatings, and geometries can provide valuable insights for optimizing heat sink performance. In addition, computational fluid dynamics (CFD) simulations can complement experimental studies by providing a detailed understanding of fluid flow and heat transfer phenomena within the heat sink channels.

CRediT authorship contribution statement

Hamza Babar: Data curation, Formal analysis, Validation, Visualization, Investigation, Methodology, Writing – original draft. **Hongwei Wu:** Supervision, Conceptualization, Writing – review & editing. **Wenbin Zhang:** Supervision, Conceptualization, Writing – review & editing.

Declaration of Competing Interest

The authors declare that they have no known competing financial interests or personal relationships that could have appeared to influence the work reported in this paper.

Data availability

Data will be made available on request.

Acknowledgment

The authors would like to acknowledge the financial support from the Engineering and Physical Science Research Council (EPSRC), UK (Grant No. EP/X038319/1).

References

[1] R. Bhuiya, N. Shah, D. Arora, N.V. Krishna, S. Manikandan, C. Selvam, R. Lamba, Thermal management of phase change material integrated thermoelectric cooler with different heat sink geometries, J. Energy Storage 51 (2022), 104304, https://doi.org/10.1016/j.est.2022.104304.

[2] R. Kalbasi, Introducing a novel heat sink comprising PCM and air - Adapted to electronic device thermal management, Int. J. Heat Mass Transf. 169 (2021), https://doi.org/10.1016/j.ijheatmasstransfer.2021.120914.

[3] M. Sheikholeslami, Numerical analysis of solar energy storage within a double pipe utilizing nanoparticles for expedition of melting, Sol. Energy Mater. Sol. Cells 245 (2022), 111856, https://doi.org/10.1016/j.solmat.2022.111856.

[4] D.S. Jang, S. Yun, S.H. Hong, W. Cho, Y. Kim, Performance characteristics of a novel heat pipe-assisted liquid cooling system for the thermal management of lithium-ion batteries, Energy Convers. Manag. 251 (2022), 115001, https://doi.org/10.1016/j.enconman.2021.115001.

[5] S. Wu, K. Zhang, G. Song, J. Zhu, B. Yao, Experimental study on the performance of a tree-shaped mini-channel liquid cooling heat sink, Case Stud. Therm. Eng. 30 (2022), 101780, https://doi.org/10.1016/j.csite.2022.101780.

[6] M. Gorzin, A.A. Ranjbar, M.J. Hosseini, Experimental and numerical investigation on thermal and hydraulic performance of novel serpentine minichannel heat sink for liquid CPU cooling, Energy Rep. 8 (2022) 3375–3385, https://doi.org/10.1016/j.egyr.2022.02.179.

[7] H. Wang, Z. Chen, J. Gao, Influence of geometric parameters on flow and heat transfer performance of micro-channel heat sinks, Appl. Therm. Eng. 107 (2016) 870–879, https://doi.org/10.1016/j.applthermaleng.2016.07.039.

[8] M.U. Sajid, H.M. Ali, A. Sufyan, D. Rashid, S.U. Zahid, W.U. Rehman, Experimental investigation of TiO2–water nanofluid flow and heat transfer inside wavy mini-channel heat sinks, J. Therm. Anal. Calorim. 137 (2019) 1279–1294, https://doi.org/10.1007/s10973-019-08043-9.

[9] M. Sheikholeslami, Z. Ebrahimpour, Thermal improvement of linear Fresnel solar system utilizing Al2O3-water nanofluid and multi-way twisted tape, Int. J. Therm. Sci. 176 (2022), 107505, https://doi.org/10.1016/j.ijthermalsci.2022.107505.

[10] M.U. Sajid, H.M. Ali, Y. Bicer, Exergetic performance assessment of magnesium oxide–water nanofluid in corrugated minichannel heat sinks: an experimental study, Int. J. Energy Res. 46 (2022) 9985–10001, https://doi.org/10.1002/er.6024.

[11] R. Ajith Krishnan, K.R. Balasubramanian, S. Suresh, The effect of heating area orientation on flow boiling performance in microchannels heat sink under subcooled condition, Int. J. Heat Mass Transf. 110 (2017) 276–293, https://doi.org/10.1016/j.ijheatmasstransfer.2017.03.030.

[12] X.L. Xie, Z.J. Liu, Y.L. He, W.Q. Tao, Numerical study of laminar heat transfer and pressure drop characteristics in a water-cooled minichannel heat sink, Appl. Therm. Eng. 29 (2009) 64–74, https://doi.org/10.1016/j.applthermaleng.2008.02.002.

[13] S.I. Koshoridze, Y.K. Levin, Bubble formation on a hydrophobic surface, Tech. Phys. 65 (2020) 846–850, https://doi.org/10.1134/S1063784220060171.

[14] G. Pan, B. Yang, Effect of surface hydrophobicity on the formation and stability of oxygen nanobubbles, ChemPhysChem 13 (2012) 2205–2212, https://doi.org/10.1002/cphc.201100714.

[15] J. Yang, J. Duan, D. Fornasiero, J. Ralston, Very small bubble formation at the solid-water interface, J. Phys. Chem. B 107 (2003) 6139–6147, https://doi.org/10.1021/jp0224113.

[16] T. Dixit, I. Ghosh, Review of micro- and mini-channel heat sinks and heat exchangers for single phase fluids, Renew. Sustain. Energy Rev. 41 (2015) 1298–1311, https://doi.org/10.1016/j.rser.2014.09.024.

[17] M. Sheikholeslami, Z. Khalili, Investigation of solar photovoltaic-thermoelectric system for building unit in presence of helical tapes and jet impingement of hybrid nanomaterial, J. Build. Eng. 74 (2023), 106871, https://doi.org/10.1016/j.jobe.2023.106871.

[18] S. Naderizadeh, A. Athanassiou, I.S. Bayer, Interfacing superhydrophobic silica nanoparticle films with graphene and thermoplastic polyurethane for wear/abrasion resistance, J. Colloid Interface Sci. 519 (2018) 285–295, https://doi.org/10.1016/j.jcis.2018.02.065.

[19] A. Amudha, H.D. Shashikala, O.S. Asiq Rahman, A.K. Keshri, H.S. Nagaraja, Effect of graphene oxide loading on plasma sprayed alumina-graphene oxide composites for improved anticorrosive and hydrophobic surface, Surf. Topogr. 7 (2019), 024003, https://doi.org/10.1088/2051-672X/ab2707.

[20] J. Durret, N. Frolet, C. Gourgon, Hydrophobicity and anti-icing performances of nanoimprinted and roughened fluoropolymers films under overcooled temperature, Microelectron. Eng. 155 (2016) 1–6, https://doi.org/10.1016/j.mee.2016.01.011.

[21] M. Espanhol-Soares, L. Costa, M.R.A. Silva, F. Soares Silva, L.M.S. Ribeiro, R. Gimenes, Super-hydrophobic coatings on cotton fabrics using sol–gel technique by spray, J. Solgel Sci. Technol. 95 (2020) 22–33, https://doi.org/10.1007/s10971-020-05307-x.

[22] H. Ogihara, J. Xie, J. Okagaki, T. Saji, Simple method for preparing superhydrophobic paper: spray-deposited hydrophobic silica nanoparticle coatings exhibit high water-repellency and transparency, Langmuir 28 (2012) 4605–4608, https://doi.org/10.1021/la204492q.

[23] S.R. Hosseini, M. Sheikholeslami, M. Ghasemian, D.D. Ganji, Nanofluid heat transfer analysis in a microchannel heat sink (MCHS) under the effect of magnetic field by means of KKL model, Powder Technol. 324 (2018) 36–47, https://doi.org/10.1016/j.powtec.2017.10.043.

[24] S. Nawaz, H. Babar, H.M. Ali, M.U. Sajid, M.M. Janjua, Z. Said, A.K. Tiwari, L. S. Sundar, C. Li, Oriented square shaped pin-fin heat sink: performance evaluation employing mixture based on ethylene glycol/water graphene oxide nanofluid, Appl. Therm. Eng. 206 (2022), 118085, https://doi.org/10.1016/j.applthermaleng.2022.118085.

[25] R.K. Shah, Thermal entry length solutions for the circular tube and parallel plates, in: Proceedings of 3rd National Heat and Mass Transfer Conference, Indian Institute of Technology Bombay Delhi, 1975, pp. 11–75.

[26] N. Ahammed, L.G. Asirvatham, S. Wongwises, Thermoelectric cooling of electronic devices with nanofluid in a multiport minichannel heat exchanger, Exp. Therm Fluid Sci. 74 (2016) 81–90, https://doi.org/10.1016/j.expthermflusci.2015.11.023.

[27] A. Qamar, R. Shaukat, S. Imran, M. Farooq, M. Amjad, Z. Anwar, H. Ali, M. Farhan, M.A. Mujtaba, T. Korakianitis, M.A. Kalam, F. Almomani, Effect of surfactants on the convective heat transfer and pressure drop characteristics of ZnO/DIW nanofluids: an experimental study, Case Stud. Therm. Eng. 42 (2023), 102716, https://doi.org/10.1016/j.csite.2023.102716.

[28] S.K. Oudah, A. Tikadar, R. Fang, K. Egab, J.A. Khan, Thermohydraulic characteristics of a knurled microchannel heat sink in single phase regime. ASTFE Digital Library, Begel House Inc., 2018.

[29] R. Ajith Krishnan, K.R. Balasubramanian, S. Suresh, Experimental investigation of the effect of heat sink orientation on subcooled flow boiling performance in a rectangular microgap channel, Int. J. Heat Mass Transf. 120 (2018) 1341–1357, https://doi.org/10.1016/j.ijheatmasstransfer.2017.12.133.

[30] M. Liu, D. Liu, S. Xu, Y. Chen, Experimental study on liquid flow and heat transfer in micro square pin fin heat sink, Int. J. Heat Mass Transf. 54 (2011) 5602–5611, https://doi.org/10.1016/j.ijheatmasstransfer.2011.07.013.

[31] H. Babar, H. Wu, H.M. Ali, T.R. Shah, W. Zhang, Staggered oriented airfoil shaped pin-fin heat sink: investigating the efficacy of novel water based ferric oxide-silica

hybrid nanofluid, Int. J. Heat Mass Transf. 194 (2022), 123085, https://doi.org/10.1016/j.ijheatmasstransfer.2022.123085.
[32] A. Kosar, C.J. Kuo, Y. Peles, Hydoroil-based micro pin fin heat sink, in: Proceedings of the IMECE, 2008, pp. 563–570, https://doi.org/10.1115/imece2006-13257.
[33] Z. Azizi, A. Alamdari, M.R. Malayeri, Thermal performance and friction factor of a cylindrical microchannel heat sink cooled by Cu-water nanofluid, Appl. Therm. Eng. 99 (2016) 970–978, https://doi.org/10.1016/j.applthermaleng.2016.01.140.
[34] Z. Feng, X. Luo, F. Guo, H. Li, J. Zhang, Numerical investigation on laminar flow and heat transfer in rectangular microchannel heat sink with wire coil inserts, Appl. Therm. Eng. 116 (2017) 597–609, https://doi.org/10.1016/j.applthermaleng.2017.01.091.
[35] M.W. Uddin, N.S. Sifat, Comparative study on hydraulic and thermal characteristics of minichannel heat sink with different secondary channels in parallel and counter flow directions, Int. J. Thermofluids 17 (2023), 100296, https://doi.org/10.1016/j.ijft.2023.100296.
[36] R. Kumar, B. Tiwary, P.K. Singh, Thermofluidic analysis of Al2O3-water nanofluid cooled branched wavy heat sink, Appl. Therm. Eng. 201 (2022), 117787, https://doi.org/10.1016/j.applthermaleng.2021.117787.
[37] L. Chai, G. Xia, M. Zhou, J. Li, J. Qi, Optimum thermal design of interrupted microchannel heat sink with rectangular ribs in the transverse microchambers, Appl. Therm. Eng. 51 (2013) 880–889, https://doi.org/10.1016/j.applthermaleng.2012.10.037.
[38] Y. Fan, P.S. Lee, L.W. Jin, B.W. Chua, D.C. Zhang, A parametric investigation of heat transfer and friction characteristics in cylindrical oblique fin minichannel heat sink, Int. J. Heat Mass Transf. 68 (2014) 567–584, https://doi.org/10.1016/j.ijheatmasstransfer.2013.09.027.
[39] H.T. Phan, Effects of Nano and Micro-Surface Treatments on Boiling Heat Transfer, Institut National Polytechnique de Grenoble - INPG, 2010. https://theses.hal.science/tel-00574573.
[40] X. Wang, S. Zhao, H. Wang, T. Pan, Bubble formation on superhydrophobic-micropatterned copper surfaces, Appl. Therm. Eng. 35 (2012) 112–119, https://doi.org/10.1016/j.applthermaleng.2011.10.012.
[41] A. Agarwal, An Experimental Study of Nanobubbles On Hydrophobic Surfaces, Massachusetts Institute of Technology, 2005 dspace.mit.edu/handle/1721.1/7582 (accessed July 8, 2023).
[42] S. Yang, S.M. Dammer, N. Bremond, H.J.W. Zandvliet, E.S. Kooij, D. Lohse, Characterization of nanobubbles on hydrophobic surfaces in water, Langmuir 23 (2007) 7072–7077, https://doi.org/10.1021/la070004i.
[43] N. Canter, Presence of nanobubbles on superhydrophobic surfaces, Tribol. Lubr. Technol. 66 (2010) 14.
[44] N.H. Naqiuddin, L.H. Saw, M.C. Yew, F. Yusof, H.M. Poon, Z. Cai, H.S. Thiam, Numerical investigation for optimizing segmented micro-channel heat sink by Taguchi-Grey method, Appl. Energy 222 (2018) 437–450, https://doi.org/10.1016/j.apenergy.2018.03.186.